Afterslip of the M w 8.3 2015 Illapel Earthquake Imaged Through a Time-Dependent Inversion of Continuous and Survey GNSS Data

R. Tissandier, J.-M. Nocquet, E. Klein, C. Vigny, J. Ojeda, S. Ruiz

JGR Solid Earth

RESEARCH ARTICLE
10.1029/2022JB024778

Afterslip of the M_w 8.3 2015 Illapel Earthquake Imaged Through a Time-Dependent Inversion of Continuous and Survey GNSS Data

R. Tissandier[1], J.-M. Nocquet[1,2], E. Klein[3], C. Vigny[3], J. Ojeda[1,4], and S. Ruiz[4]

[1]Université de Paris, Institut de physique du globe de Paris, CNRS, Paris, France, [2]Université Côte d'Azur, IRD, CNRS, Observatoire de la Côte d'Azur, Sophia Antipolis, France, [3]Laboratoire de géologie – CNRS UMR, École normale supérieure – PSL University, Paris 8538, France, [4]Departamento de Geofísica, Universidad de Chile, Santiago, Chile

Key Points:

- A full time-dependent inversion provides a detailed view of afterslip during the 2.5 months following the Illapel earthquake in Chile
- Afterslip developed at three preferential areas, one of which overlaps a region of significant coseismic slip (2–4 m)
- Afterslip shows local and short-term acceleration after large aftershocks and a slow slip event

Supporting Information:

Supporting Information may be found in the online version of this article.

Correspondence to:

R. Tissandier,
tissandier@ipgp.fr

Citation:

Tissandier, R., Nocquet, J.-M., Klein, E., Vigny, C., Ojeda, J., & Ruiz, S. (2023). Afterslip of the M_w 8.3 2015 Illapel earthquake imaged through a time-dependent inversion of continuous and survey GNSS data. *Journal of Geophysical Research: Solid Earth*, *128*, e2022JB024778. https://doi.org/10.1029/2022JB024778

Received 16 MAY 2022
Accepted 14 JAN 2023

Author Contributions:

Conceptualization: J.-M. Nocquet, E. Klein, C. Vigny
Formal analysis: R. Tissandier
Investigation: R. Tissandier
Methodology: J.-M. Nocquet
Software: J.-M. Nocquet
Validation: R. Tissandier, J.-M. Nocquet
Visualization: R. Tissandier
Writing – original draft: R. Tissandier
Writing – review & editing: R. Tissandier, J.-M. Nocquet, E. Klein, C. Vigny, J. Ojeda, S. Ruiz

Abstract

We use continuous and survey GNSS data to image the spatial and temporal evolution of afterslip during the 2 months following the M_w 8.3 2015 Illapel earthquake. Our approach solves for the incremental daily slip at the subduction interface using nonnegative least squares with spatial and temporal Laplacian regularization constraints. We find that afterslip developed at three specific areas at the megathrust, surrounding the coseismic rupture. In addition, well resolved afterslip also occurs within the coseismic rupture area that experienced ∼4 m of seismic slip. Our afterslip model shows striking correlations with the spatial distribution of aftershocks and repeating earthquakes. We capture the local afterslip triggered by a M_w 6.8 and two 6.9 aftershocks that ruptured downdip and north of the coseismic rupture, respectively. The latter ones were possibly triggered by the afterslip that developed north of the rupture. We also find a pulse of enhanced aseismic slip lasting a few days south of the rupture that spatially and temporally correlates with a seismicity burst. We finally find that areas of enhanced afterslip spatially correlates with areas having experienced regular seismic swarms observed during the years *prior* to the Illapel earthquake. This correlation supports the view of localized fluid high pore pressure areas behaving aseismically and surrounding a highly locked asperity, preventing the seismic rupture to propagate into them.

Plain Language Summary

After a large earthquake, aseismic slip occurs in the vicinity of the seismic rupture. In this study, we focus on the aseismic slip that occurred after a large subduction earthquake of magnitude 8.3 in 2015 in central Chile. Using GPS time series, we obtain a spatiotemporal view of the aseismic slip during the 2 months following the earthquake. We find that aseismic slip occurred at three preferential areas located at the periphery of the rupture, as observed for many earthquakes. However, we also identify a patch of aseismic slip within the rupture area. We could image the daily afterslip rate and compare it to the daily seismicity and found striking correlations with the spatial distribution of aftershocks. In particular, we find that the largest aftershocks with magnitude 6.8–6.9 are tightly related to the evolution of afterslip. This result suggests that precisely monitoring the evolution of afterslip after a large earthquake might help to define preferential areas of large aftershocks. We also find a potential slow slip event south of the mainshock rupture which correlates with a local increase of seismicity. Finally, we find that the areas of enhanced afterslip had experienced seismic swarms decades before the earthquake, possibly reflecting areas of the fault with high fluid pore pressure. These results highlight new aspects about the dynamics of afterslip.

1. Introduction

During the weeks following a large earthquake, transient aseismic slip, referred as afterslip, develops at the fault and dominates the deformation observed at the Earth' surface. The development of continuous GNSS networks at subduction zones for almost three decades has allowed to capture the main pattern of the afterslip that followed some major megathrust events: afterslip initiates immediately after the earthquake, with a slip rate decreasing through time as $\frac{1}{t}$ leading to a logarithmic growth of the cumulative slip (*e.g.*, Perfettini et al., 2010). Afterslip takes place at areas of the fault surrounding the coseismic rupture (Perfettini et al., 2010), with little if any slip inside the coseismic rupture. The evolution of the cumulative number of aftershocks mimics the afterslip evolution both in time and space, and the moment released through aftershocks is only a small fraction of the afterslip equivalent moment (Hsu et al., 2006; Perfettini & Avouac, 2004).

Afterslip has been interpreted as the frictional response of the fault to the stress increment induced by the earthquake at the area surrounding the coseismic slip. In a rate-and-state friction framework, areas experiencing afterslip are supposed to follow a rate-strengthening regime where friction increases with the sliding velocity (Avouac, 2015; Lay & Kanamori, 1981). Specifically, rate-strengthening law successfully predicts the logarithmic evolution of the cumulated afterslip. First order comparison between the location of areas that are locked during the interseismic phase, the location of the seismic rupture and afterslip support a view where the fault is composed of locked patches accumulating slip deficit released through seismic ruptures, embedded in an overall slipping and aseismic fault plane (Avouac, 2015; Lay & Kanamori, 1981).

However, despite the overall success of the above "rate-state asperity model" in explaining the main pattern of afterslip, there are several observations that suggest a more complex view. For a few cases, afterslip and aftershocks have been found to be located within the coseismic rupture area (Agurto et al., 2012; Bedford et al., 2013; Johnson et al., 2012; Tsang et al., 2019). Some afterslip has also been found at areas locked during the years *prior* the earthquake (Rolandone et al., 2018). Finally, afterslip develops at specific locations rather than as a rim surrounding the coseismic rupture as would be expected from the coseismic stress increment (Bedford et al., 2013; Perfettini et al., 2010; Rolandone et al., 2018).

Finally, some studies argued that Slow Slip Events (SSEs) during the interseismic period and areas of afterslip take place at the same locations (Hobbs et al., 2017; Rolandone et al., 2018). Those results question the friction law and the processes that could simultaneously explain the spontaneous occurrence of SSE during the interseismic phase and afterslip. A related open question is to know whether we can observe some modulation of the afterslip rate, that would be superimposed to the overall long-term afterslip decay. Such a behavior has been proposed by Bedford et al. (2013) for the 2010 M_w 8.8 Maule earthquake, where the inversion of GNSS data shows several pulses of aseismic slip during 2.5–9 months after the mainshock. However, such pulses have not been documented for others large megathrust events.

1.1. Previous Works on the 2015 Illapel Earthquake

With a good GNSS data coverage and a coastline located ∼70 km away from the trench, the September 16, 2015 M_w 8.3 Illapel earthquake offers a good opportunity for a detailed study of afterslip time evolution following a large megathrust earthquake. It ruptured a 200 km long segment of the megathrust along the Nazca/South America subduction in Chile. The Illapel segment experiences regular M8+ earthquakes every 60–80 years (*i.e.*, 1880, 1943, and 2015), and is thought to be the northern segment of the 1730 $M \sim 9$ great earthquake with a proposed rupture length exceeding 500 km (Ruiz & Madariaga, 2018). Coseismic slip models consistently find a maximum slip of 8–10 m, with several meters of slip reaching the trench, attested by a significant tsunami (Barnhart et al., 2016; Klein et al., 2017; Melgar et al., 2016; Ruiz et al., 2016; Shrivastava et al., 2016). All coseismic slip models also find that large slip (>5m) remained confined within the first shallowest ∼35 km. They however also highlight that several meters of seismic slip extended downdip to ∼55 km depth along a 50 km wide portion of the megathrust at latitude 31°S (Figure 1).

Previous studies used different data sets, time periods, and methodology to estimate the afterslip. The early stage of afterslip (hours to 3 days) was studied by Twardzik et al. (2021) and Liu et al. (2022), using kinematic GNSS data and successive static inversions through time. Both studies found two patches of afterslip, surrounding the northern and the southern deep edges of the mainshock rupture, but highlighted some peculiar behaviors of the early afterslip. Liu et al. (2022) found that the rapid displacement evolution observed at GNSS site CNBA (Figure 1) evolves as a power law, rather than the usual logarithmic model. However, Twardzik et al. (2021) found that the coseismic slip associated with large aftershocks (up to M_w 7.1) for the southern patch (close to CNBA) can explain all the geodetically determined slip during the first 12 hr for that area. This result highlights that locally, seismic slip through large aftershocks can significantly contribute to the total slip and certainly impact the afterslip evolution.

After the early stage, several studies based on daily GNSS solutions and InSAR results concurrently find that afterslip develops from two discrete areas located along the northern and southern edges of the coseismic rupture. The two areas of afterslip are separated by the deepest portion of the coseismic rupture (Barnhart et al., 2016; Feng et al., 2017; Huang et al., 2017; Shrivastava et al., 2016). Detailed studies of the aftershock sequence show that aftershocks are mainly located at or close to areas experiencing large afterslip (Huang et al., 2017). Frank

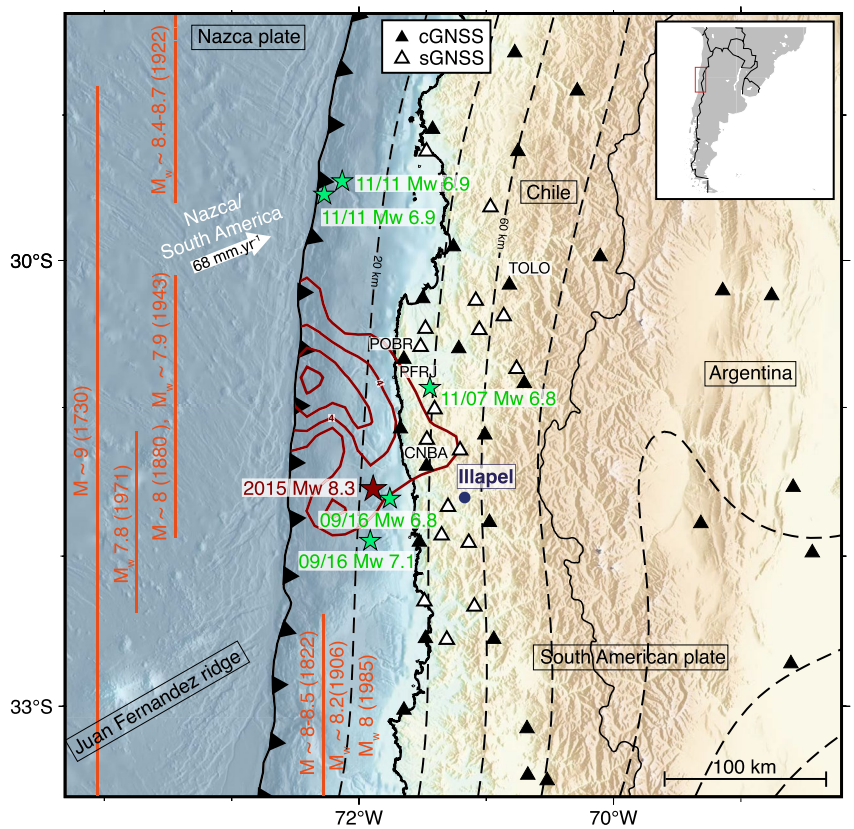

Figure 1. GNSS network used in this study and past megathrust earthquakes. Black and white triangles are permanent and survey GNSS sites, respectively. The green stars are the large aftershocks epicenters ($M_w \geq 6.8$) of the Illapel earthquake (CSN catalog). The red curves indicate the Illapel 2015 M_w 8.3 coseismic slip distribution contoured every 2 m (Klein et al., 2017). The red star is the Illapel earthquake epicenter. The orange lines indicate the proposed lateral extent of historical and recent megathrust earthquakes (Ruiz & Madariaga, 2018). The dashed lines are the Slab2.0 isodepth contours every 20 km (Hayes et al., 2018).

et al. (2017) and Liu et al. (2022) further find that the aftershock and afterslip areas are spreading along strike through time, an observation which is consistent with the prediction for rate-strengthening areas response to a coseismic Coulomb stress increment.

Although these observations agree with the "rate-state asperity" model, there are also several characteristics that challenge that view. A peculiar feature is the absence of significant afterslip downdip the deepest part of the rupture (at latitude 31.2°S, 50 km depth). There is also no afterslip at shallow depth (<10 km) from latitude 30.8°S along the southern edge of the coseismic rupture. In addition, for most models, part of the afterslip overlaps with areas having slipped seismically by 3–6 m during the mainshock (Barnhart et al., 2016; Shrivastava et al., 2016).

In this study, we aim at precisely characterizing the spatial evolution of afterslip following the Illapel earthquake. For that purpose, we perform a full time-dependent inversion of the daily slip from GNSS time series, including both continuous and survey measurements. While previous studies have described the cumulative afterslip evolution, our approach focuses on the dynamic of afterslip over periods of a few days. In particular, we investigate whether afterslip smoothly increases through time as a logarithmic function or whether slip pulses or modulations can be identified. We specifically compare our model with the seismicity rate evolution and investigate the relationship between afterslip and the occurrence of the largest aftershocks.

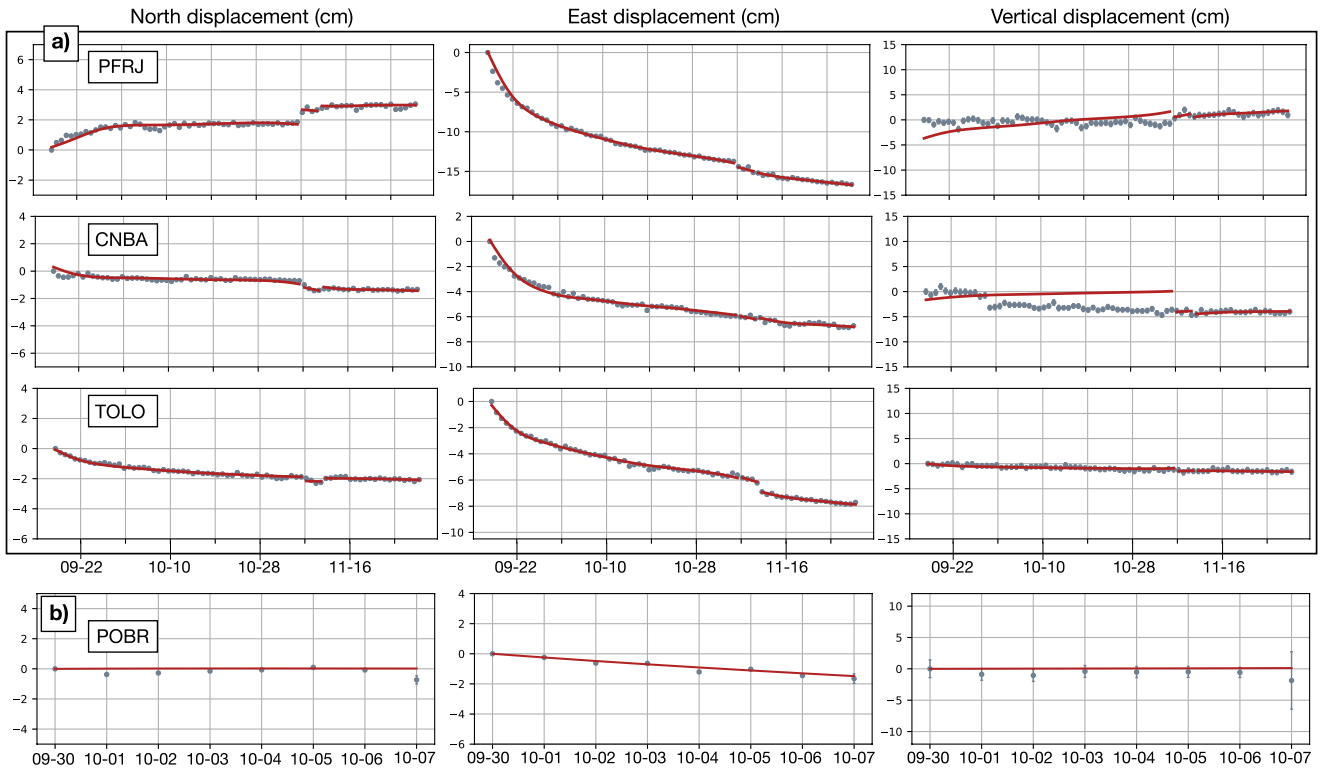

Figure 2. Observed and modeled time series at selected sites located in Figure 1. (a) continuous GNSS (cGNSS) sites PFRJ, CNBA, TOLO and (b) survey GNSS (sGNSS) site POBR. Left column is the north component, middle column is the east component, and right column is the vertical component. The gray dots indicate the daily displacement since the first date of observation together with the $1-\sigma$ error bar. The red curve shows the modeled time series according to our preferred afterslip model.

2. Data

2.1. Data

Our input data set is composed of 28 continuous GNSS (cGNSS) sites and 17 survey (sGNSS) sites (Figure 1 and Figure S1 in Supporting Information S1). cGNSS sites in the Illapel area were installed by the joint international laboratory (LIA) Montessus de Ballore (Vigny et al., 2009) and are now operated by the Centro Sismológico Nacional (CSN, Universidad de Chile, Santiago, Baez et al., 2018). Six cGNSS sites are located in Argentina and are part of the Red Argentina de Monitoreo Satelital Continuo (RAMSAC, Piñón et al., 2018). We use the cGNSS time series from the processing SOAM_GNSS_solENS solution described in Klein et al. (2022). Postseismic time series are obtained by removing the interseismic velocity before the Illapel earthquake estimated from 4 years of data with the MIDAS method of Blewitt et al. (2016).

The selected cGNSS network used in this study (see Figure 1) spreads ~150 km along strike north and south of the coseismic rupture and ~400 km inland from the trench. Twenty-two cGNSS sites recorded data during the whole period of our study from September 17 to November 31 (74 days), while six of them provided approximately a month and a half of data. Two large aftershocks (M_w 7.1 and M_w 6.8) ruptured within the 6 hr that followed the mainshock south of the epicenter (Figure 1) causing a few centimeters displacements (Twardzik et al., 2021). Our first observation corresponds to the 24 hr average position during day September 17, mitigating the potential bias induced by the aftershocks on the first position. The cGNSS data are complemented by 17 sGNSS sites reoccupied after the Illapel earthquake and provide 4–9 days of measurements, between September 27, 2015 and November 30, 2015. sGNSS sites bring additional information because postseismic daily displacements were still of the order of several millimeters per day during the survey period (Figure 2b), larger than the daily position uncertainty. Among the sGNSS data used, five sites are located in the immediate vicinity of the mainshock rupture and seven others are located less than 50 km from the rupture edge, providing dense measurements above the downdip limit of the coseismic rupture. Compared to previous studies, these sGNSS sites

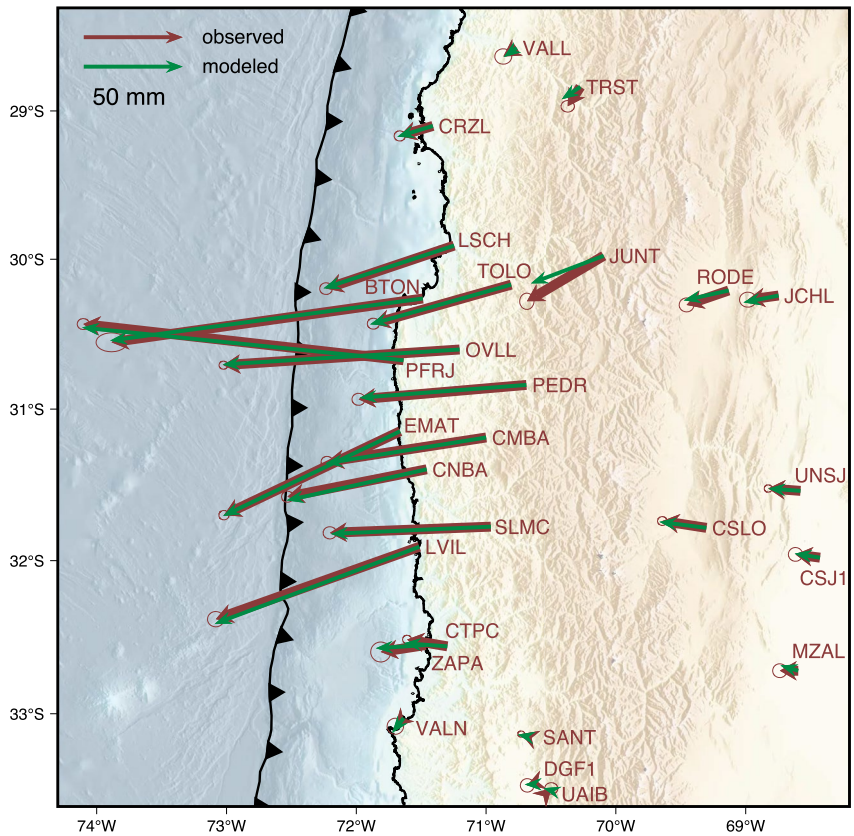

Figure 3. Observed (brown) and modeled (green) GNSS cumulative horizontal displacements on November 30, 2015, 74 days after the mainshock. Error ellipses are $1-\sigma$ confidence level.

provide additional constraints on the afterslip evolution during their observation period, contributing to make the model more robust.

2.2. Time Series Patterns

After the Illapel earthquake, cGNSS times series show logarithm-like, rapid, postseismic displacements on the east component during the first 2 weeks following the mainshock (Figures 2 and 3). The westward displacement reaches 10 cm at PFRJ and 5 cm at CNBA close to the rupture (Figure 1). Located one hundred kilometers north of the rupture area, cGNSS site TOLO shows almost as much displacement as CNBA, suggesting a large amount of afterslip north of the rupture.

As an example, Figure 2 shows the time series at survey site POBR which was installed on 30 September 2015, 2 weeks after the earthquake north of the rupture. POBR shows almost 2 cm of westward displacement during a week period, demonstrating the interest of including sGNSS data in afterslip modeling.

The GNSS network also recorded the coseismic displacements of the largest aftershocks of the sequence. The first one was a M_w 6.8 earthquake and ruptured on November 7 (51 days after the mainshock) at ~40 km depth. The others were two M_w 6.9 earthquakes that occurred on November 11 (55 days after the mainshock) at shallow depth close to the trench, ~100 km north of the rupture. In order to investigate the relationship between the afterslip and the occurrence of those earthquakes, for both dates, we extracted the coseismic offsets and invert for the coseismic slip spatial distribution (see Figure S6 in Supporting Information S1).

3. Time-Dependent Modeling of the Postseismic Deformation

3.1. Method

The afterslip of the Illapel earthquake has been studied using static inversions of GNSS displacement observed at successive dates (Barnhart et al., 2016; Feng et al., 2017; Xiang et al., 2021). Although static inversion is useful

to determine the location of afterslip, it has several drawbacks: it does not warrant that the modeled slip from two successive models is meaningful, and could for instance lead to nonphysical negative slip. This would be critical for successive dates where the observed displacement is small, close to the data noise level. Successive static inversions cannot account for possible differential displacement among sites during the period, that carry information of the path followed by the slip. Also, new GNSS sites installed after the earthquake cannot be included in the inversion because their displacement since the earthquake is unknown. In that case, a different time window can be selected, but with the difficulty of inserting the results in a consistent way in the inversion of the whole time period.

Our approach overcomes these limitations by simultaneously solving for the spatially variable daily slip rate using all available time series. It therefore includes the information of the cumulated displacement at a given date as static inversions would do, but also uses the information of the trend of the observed displacement. It further includes the constraint that incremental daily slip must be positive. Shrivastava et al. (2016) apply the PCAIM method of Kositsky and Avouac (2010) to obtain daily afterslip estimates. PCAIM uses a decomposition where spatially stationary sources are combined with a time function. Compared to PCAIM, our approach does not include the assumption that slip is a combination of spatially stationary sources. Here, we summarize the method together with the relevant information for the kinematic inversion of the Illapel afterslip.

The plate interface is discretized into 1,014 quasi-equilateral triangular subfaults with 14 km long edges (see Figure S2 in Supporting Information S1), following the curved surface from the Slab2.0 model (Hayes et al., 2018). The fault area extends from latitude 32°S to 28°S and from the trench down to 90 km depth.

The cumulative slip $s_i\,(t)$ at each subfault i at time t is parametrized as a monotonic increasing piecewise linear function of time:

$$s_i(t) = \sum_{t_k=0}^{t_k \le t} \dot{s}_i(t_k)\Delta_k \tag{1}$$

where $\dot{s}_i(t_k)$ is the constant slip rate during day k with duration $\Delta_k = 1$ day. The displacement $d_{jl}\,(t)$ observed for component j at site l is:

$$\sum_{i=1}^{n} g_{ijl}\, s_i(t) = d_{jl}(t) \tag{2}$$

where n is the number of subfaults, g_{ijl} is the Green function, here calculated in an homogeneous elastic half space for triangular dislocation (Nikkhoo & Walter, 2015). The rake is kept fixed at a value derived from the direction of the Nazca/South America plate convergence from Vigny et al. (2009). Combining Equations 1 and 2 gives the observation equation:

$$\sum_{t_k=0}^{t_k \le t} \sum_{i=1}^{n} g_{ijl}\, \dot{s}_i(t_k) = d_{jl}(t) \tag{3}$$

Stacking $\dot{s}_i(t_k)$ for all dates in a single vector $\dot{s}$, and all time series $d_{jl}\,(t)$ in vector d leads to the linear system:

$$G\,\dot{s} = d \tag{4}$$

The inverse problem associated with Equation 4 is highly underdetermined. We add regularization constraints in the form of minimum Laplacian in space and time. For that, we build a discrete Laplacian operator by setting that every $\dot{s}_i(t_k)$ equals (in the least squares sense) the weighted average of its spatial neighbor at t_k and its time neighbors at time t_{k-1} and t_{k+1}. Although applied simultaneously in the time-and-space domains, this approach allows for different spatial and temporal smoothing constraints, controlled by the dimensionless constants λ_{space} and λ_{time}, respectively. As input data, we use both horizontal and vertical displacements at GNSS sites together with their associated uncertainty rescaled to account for the observed daily scatter. Because of larger uncertainty and sensitivity to the Earth' elastic structure, the vertical component is further down-weighted by a factor of three in the inversions. This value has been empirically chosen so that the sum of the squared normalized residuals (residual divided by the standard deviation) is similar for the three components east, north and up.

Our method offers the advantage of explicitly imposing a nonnegative constraint on the inverted daily slip. The method also accepts that some data might be missing. This is particularly useful for postseismic modeling where

additional sites are often deployed several days or weeks after the mainshock. Here, for instance, it allows us to include 4–16 days of survey data in our analysis. Finally, it allows a simple handling of aftershocks without the need to correct the time series for coseismic offsets. Indeed, Equation 2 can also be written as:

$$\sum_{i=1}^{n} g_{ijl}\, s_i(t - t_a) = d_{jl}(t - t_a) \tag{5}$$

where t_a is the origin time of an aftershock. So, handling aftershocks only requires to consider a time series as two separate time series before and after an aftershock. This approach was applied in our inversion for the M_w 6.8 aftershock of November 7 and the M_w 6.9 doublet aftershocks of November 11, considered as a single event.

We apply our method to solve for the daily incremental slip from September 17, 2015 to November 30, 2015. We selected this period because it ensures that afterslip will be the dominant process with only a small viscoelastic contribution (*e.g.*, Tian et al., 2020). This period also includes the occurrence of several large aftershocks, allowing to investigate their potential relationship with afterslip.

3.2. Regularization and Choice of Model

We used two approaches to select optimal regularization parameters. The so-called L-curve approach defines the optimal trade-off between the overall model roughness and misfit to the data (Hansen, 1992). Plotting the misfit as a function of our regularization parameters defines a surface where misfit decreases as weaker regularization parameters are used. An inflexion point is searched for which smaller regularization values only result in a marginal reduction of misfit. Here, we explored a range of combination of spatial and temporal smoothness parameters and compute the misfit defined as $\chi^2 = (G\hat{s} - d)^T C_d^{-1}(G\hat{s} - d)$ for each inverted model $\hat{s}$ (Figure S3 in Supporting Information S1). The obtained surface shows sharper variation with λ_{space} leaving the choice of λ_{time} more subjective. We selected a model with $\lambda_{\text{space}} = 0.8$ and $\lambda_{\text{time}} = 5$ that we refer as the smooth model. As an alternative method to select an optimal model, we use a cross-validation approach. The cross-validation has been used to select the optimal spatial smoothing parameters for static slip inversion from geodetic data (Freymueller et al., 1994; Matthews & Segall, 1993) using the Leave-Out-One approach. We generalize this to the time-and-space case using K-Fold cross-validation, nowadays widely used in Machine Learning problems. In that approach, the data is split into K subsets of equivalent size. For a given model, the Kth subset is removed from the observations included in the inversion and the ability of the remaining data to correctly predict data of the Kth subset is evaluated by computing the Mean Square Error (MSE) defined by:

$$MSE_k = (G_k \hat{s_k} - d_k)^T C_{d_k}^{-1}(G_k \hat{s_k} - d_k)/n_{d_k} \tag{6}$$

where d_k is the vector of the observation for subset k with length n_{d_k} and $\hat{s_k}$ is the estimated model estimated without including observations d_k and G_k the submatrix of G whose lines correspond to the observations in d_k. Too smooth models provide bad fit to all data and a large value of MSE_k. Too rough models, although providing good fit to the data used in the inversion, will provide bad prediction at their spatial and temporal neighbors that were not included in the inversion. In order to reduce the dependence of MSE on the chosen tested data subset, the inversions are repeated for all k subsets, and the final MSE score is simply the mean of all MSE_k. Most studies use 5–10 subsets, ensuring that results do not depend on the chosen division of the data. Here we use $K = 9$, splitting the analyzed period into three consecutive time windows and dividing the GNSS site into three separate subsets. Thus, for each K, one third of the sites have one third of their observations removed, which are used to compute MSE_k. Results showing the MSE score as a function of λ_{space} and λ_{time} are shown in Figure 4a.

Compared with the result of the L-curve, the cross-validation approach suggests that optimal models require lower temporal smoothing, allowing rougher models in time. We select a model with $\lambda_{\text{space}} = 1$ and $\lambda_{\text{time}} = 0.1$ that we refer as the rough model (Figure 4b).

3.3. Resolution Tests

Resolution of the kinematic inversion is difficult to assess since it would require to evaluate the model resolution both in space and time. Semianalytical solutions for the *posterior* covariance and marginal probability density functions have been proposed for the case of a linear inverse problem with covariance regularization and nonnegative constraint (Nocquet, 2018). However, such approach remains computationally out of reach for the present problem which includes 75,000 parameters (1,014 subfaults × 74 days).

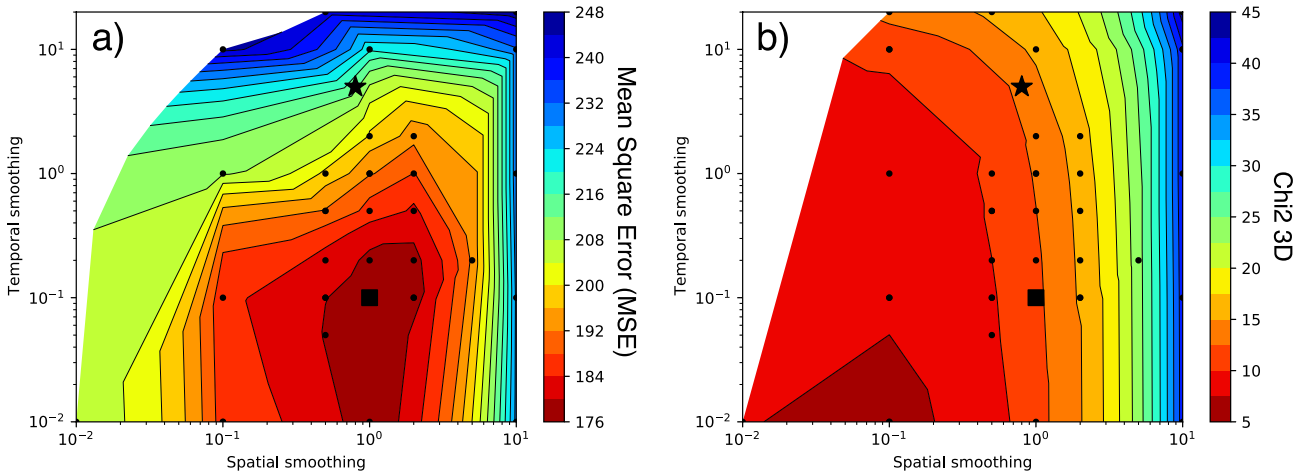

Figure 4. (a) Cross-validation and (b) L-curve. The black star is the smooth afterslip model ($\lambda_{space} = 0.8$ and $\lambda_{time} = 5$) and the black square is the rough afterslip model ($\lambda_{space} = 1$ and $\lambda_{time} = 0.1$).

In the Supporting Information S1 (see Figure S4 in Supporting Information S1), we provide static inversion checkerboard tests to evaluate the spatial resolution of our models. These tests show that patches with size of 50×50 km^2 can be resolved close to the coastline, while the resolution decreases close to the trench and to a lesser extent at depth. A kinematic inversion is expected to provide a better resolution than a static inversion at a final date of slip because the kinematic approach requires the whole history of displacement to be fitted. Hence, the tests presented in the Supporting Information S1 are probably pessimistic indicators of the true spatial resolution of the kinematic inversion results.

To get a sense of both the temporal and spatial resolution, we perform dynamic resolution tests by generating time evolving synthetic models and evaluate how well they can be retrieved in space and time. Details are provided in the Figure S5 in Supporting Information S1. A first synthetic model mimics an homogeneous logarithmic afterslip developing at a rim surrounding a fictitious circular rupture, leading to an equivalent M_w 7.5 after 20 days. This synthetic aims at evaluating the potential bias on the modeled slip due to the GNSS sites distribution and the bad sensitivity to slip occurring at shallow depth close to the trench.

We find that the kinematic inversion is able to retrieve with a good accuracy the spatial distribution of afterslip distribution, with only reduced slip close to the trench at 31.5°S (Figure S5a in Supporting Information S1). The synthetic test reveals only mild method artifacts which would erroneously concentrate the slip (Page et al., 2009). The overall time evolution is very well retrieved, as demonstrated by the similarity of the moment rate through time, with only slight underestimation of moment (Figure S5a in Supporting Information S1).

Given the good results obtained, we generate a new synthetic model by adding a slip pulse to the previous synthetic afterslip model. The synthetic slip pulse has a Gaussian spatial distribution and a Gaussian slip rate evolution through time. This model aims at evaluating whether some modulation of slip rate, small compared to the afterslip, could be retrieved by the inversion. Figure S5b in Supporting Information S1 shows the resulting inversion. Aside the overall decreasing rate, the inversion images a patch of enhanced slip, slightly spread compared to the synthetic model, but occurring at the time of the pulse.

4. Cumulative Afterslip Evolution

As a result of our time-dependent inversion, we simultaneously obtain the spatial distribution of cumulative afterslip through time and its time derivative, the afterslip rate. We first describe the evolution of the cumulative afterslip and discuss its correlation with the seismicity. Then in Section 6, we focus on the high frequency dynamics of afterslip and its relation with the large aftershocks.

4.1. Cumulative Afterslip

Both the smooth and the rough models find that afterslip initiates immediately after the mainshock at three distinct areas (Figure 5a and Movie S1 in Supporting Information S1). A first patch is located north of the

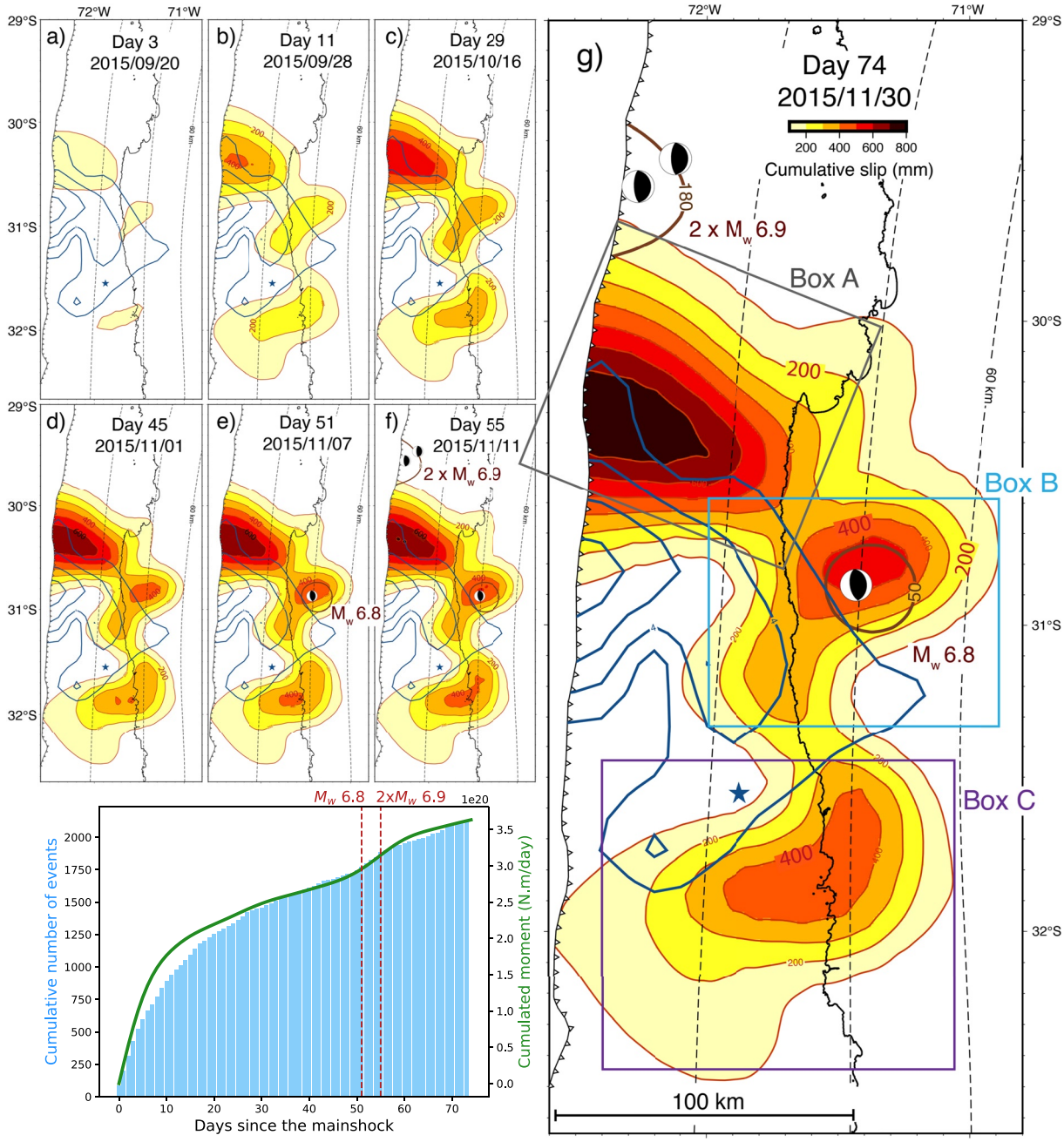

Figure 5. (a–g) Cumulative afterslip evolution (smooth model) contoured in red from 20 cm and then every 10 cm. Slip inversion results for the largest aftershocks on November 7 and November 11 are contoured in brown. Their focal mechanisms is from Global CMT (Dziewonski et al., 1981; Ekström et al., 2012). The mainshock slip is contoured in blue every 2 m (Klein et al., 2017). The blue star is the M_w 8.3 2015 Illapel epicenter. The dashed lines are the Slab2.0 isodepth contours every 20 km (Hayes et al., 2018). (h) Cumulative source time function in green and cumulative number of events (CSN catalog) as blue bars. The vertical dashed lines in red show the date of the largest aftershocks.

coseismic rupture at relatively shallow depth (~0–20 km, Box A, Figures 5a–5g). The two other patches of slip (Boxes B and C) develop at greater depth (~40 km) on the interface, on each side north and south of the deepest part of the coseismic rupture (Figures 5a–5g).

At a first order, the three areas of slip take place along the edges of the coseismic rupture, but do not perfectly surround it. More specifically, our results, with denser data, confirm that no afterslip developed downdip of the coseismic rupture at depth greater than 60 km. Overall, the pattern of afterslip shows significant north-south

asymmetry in the amount of afterslip. Indeed, as also found in previous studies, the northern patch (Box A in Figure 5g) appears to be the largest, both in size and amount of slip (Barnhart et al., 2016; Huang et al., 2017; Xiang et al., 2021). Its size is 80 km along dip and 70 km along strike, about twice the size of the deeper patches (Boxes B and C in Figure 5g). The cumulative slip at Box A reaches 50 cm after a month and exceeds 80 cm after 74 days, while it is 50 and 40 cm for the Boxes B and C, respectively, at the end of the studied period. Hence, slip in Box A contributes to 70% of the moment released through aseismic slip during the 74 days. Our inversion finds slip occurring at shallow depth, reaching the trench while previous studies found it to be restricted deeper than 10 km. Given the large distance from the GNSS sites, the shallowest afterslip cannot be well resolved. The observed difference among afterslip models, aside the different data sets, most probably reflects the impact of different regularization constraints. It however shows that a model involving shallow afterslip reaching the trench in Box A is allowed by the data.

As also found in previous studies (Barnhart et al., 2016; Feng et al., 2017; Liu et al., 2022; Shrivastava et al., 2016; Twardzik et al., 2021; Xiang et al., 2021), the shallowest part of Box B appears to overlap with an area of significant (2–4 m) coseismic slip. This latter area is close to the coast which hosts several GNSS sites, making this result robust. Box C shows similar size and slip as Box B, with a propagation of slip southward away from the rupture occurring during the first 10 days (see Movie S1 in Supporting Information S1). Box C is located where the two early aftershocks (M_w 7.1 and 6.8) occurred within the first 6 hr after the mainshock. The early afterslip imaged by the inversion at this area must also include the afterslip of these early aftershocks.

Overall, after 74 days, taking a shear modulus of 30 GPa, the moment released by the afterslip is 3.53×10^{20} N.m, equivalent to a M_w 7.6 (Figure 5h), which represents approximately 13% of the seismic moment released by the M_w 8.3 Illapel earthquake. The cumulative moment and cumulative number of aftershocks show a similar time evolution (Figure 5h), as commonly found for other earthquakes (*e.g.*, Hsu et al., 2006; Perfettini et al., 2010).

4.2. Comparison of Cumulative Afterslip With Seismicity

The aftershock sequence following the Illapel earthquake has been studied in great details, offering the opportunity for further tests of the dynamics of slip at specific locations along the plate interface. For comparison with our model, we used two different studies of seismicity. Huang et al. (2017) used a template matching approach to produce an improved earthquake catalog during a 1 month period following the mainshock (September 16, 2015 to October 16, 2015). From this catalog, they extracted 291 sequences of repeating earthquakes. They used the empirical relation between repeaters' seismic moment and aseismic slip from Nadeau and Johnson (1998) to derive estimates of incremental aseismic slip occurring along the fault. These increments of slip are then summed to provide a map of the cumulative aseismic slip, hereafter referred as repeater afterslip model. Frank et al. (2017) used the waveforms of earthquakes from the CSN catalog (Baez et al., 2018) and applied a matched-filter search for additional earthquakes. They obtained a catalog including more than 16,000 events spanning 19 months, from January 1, 2015 to June 27, 2016, covering the period analyzed in our study.

At a first order, our geodetic afterslip model, the repeater afterslip model and the density map of aftershocks all show very similar spatial patterns, outlining a crescent-shaped area surrounding the coseismic rupture with a strip of slip and aftershocks crossing the deep extent of the coseismic rupture (Figures 6a–6c). The observed spatial correlations between the geodetic afterslip models, the repeater afterslip model and the aftershocks spatial distribution are much better than any previous published models of afterslip derived from geodetic data (Barnhart et al., 2016; Huang et al., 2017; Shrivastava et al., 2016).

Our geodetic afterslip models and the repeater afterslip model consistently find that both the slip amount and the moment release are significantly larger in Box 1 north of the coseismic rupture than in Boxes 2 and 3 (Figures 6a and 6b). The density of aftershocks from Frank et al. (2017) catalog does not highlight a significantly higher aftershock activity at Box 1 (Figure 6c). On the contrary, it finds more aftershocks taking place at Box 3, perhaps because of a large number of aftershocks in this area during the first hours following the mainshock (Twardzik et al., 2021). Some spatial correlations between our models and the repeater afterslip model for some details are striking (Figures 6a and 6b), like the southernmost extension of afterslip in Box 3 or the overall southwest-northeast orientation of the slip area of Box 3.

There are also some noticeable differences. In terms of relative slip between the three areas of afterslip, Huang et al. (2017) model find that Box 3 experiences more slip than Box 2 while they are similar in our model (Figures 6a and 6b). This is perhaps also due to the contribution of aftershocks during the first hours following

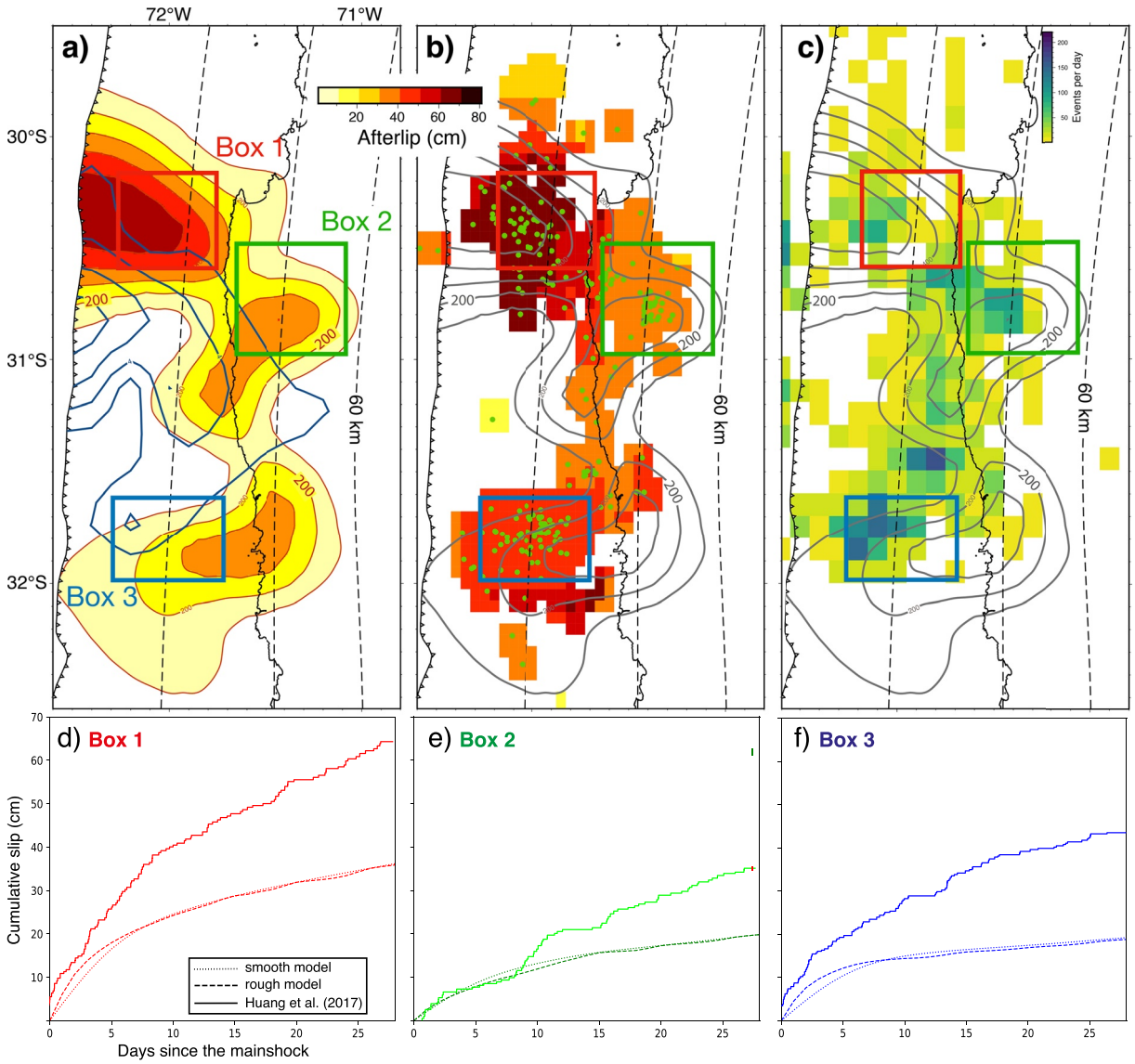

Figure 6. Comparison of (a) the 30 days cumulative afterslip smooth model contoured in red every 20 cm with (b) Huang et al. (2017) repeater afterslip model and (c) the first 30 days of Frank et al. (2017) earthquakes catalog (following the mainshock). The Boxes are identical to Huang et al. (2017) and differ from Figure 5g. The green dots are the repeater earthquakes locations of Huang et al. (2017). The mainshock slip is contoured in blue every 2 m (Klein et al., 2017). The dashed lines are the Slab2.0 depths every 20 km (Hayes et al., 2018). Comparison of the slip rate evolution of our afterslip models with Huang et al. (2017) repeater afterslip model within (d) Box 1, (e) Box 2, and (f) Box 3.

the mainshock (Twardzik et al., 2021), a pattern that our inversions cannot capture because they use 24 hr averaged data, starting the day following the mainshock.

The overall good spatial correlation found between the geodetic afterslip models with aftershocks confirms the view that afterslip drives the seismicity evolution and the repeated failure of small asperities (Figure 6). However, the comparison of seismicity with our afterslip models suggests that areas of higher aftershock activity are located at the edges of high afterslip areas rather than centered at the maximum slip areas (Figure 6c). This pattern can clearly be seen for the southern patch (Box 3 in Figure 6c) where patches with higher density of aftershocks are located updip of high afterslip patches. To a lesser extent, a similar pattern is observed for the northern and deeper patches (Figure 6c). The comparison with the repeater afterslip model also suggests that repeaters were preferentially activated at the periphery of high afterslip patches (Figure 6b). We acknowledge that the observed spatial correlation between slip gradient and aftershock/repeater activity cannot be demonstrated given (a) our resolution tests, (b) the location uncertainty of aftershocks, and (c) the spatial averaging choice (0.15° × 0.15°

wide cells) used in the repeater afterslip model (Huang et al., 2017). Nonetheless, our comparison shows that such a correlation is compatible with the data and also compatible with a physical model where aftershocks occur as the result of increased shear stress at the interface induced by nearby aseismic slip, as proposed in Chalumeau et al. (2021). In terms of slip amount, the repeater afterslip model is sensibly higher than our afterslip models (Figures 6a and 6b).

Now focusing on the temporal evolution, Figure 5h confirms an overall agreement between the evolution of the cumulative afterslip and the cumulative number of aftershocks. In an attempt to evaluate potential finer correlation, Figures 6d–6f show the cumulative slip evolution for the repeater afterslip model calculated by Huang et al. (2017) at three different areas (Boxes 1–3 in Figure 6a) together with our geodetic afterslip model prediction during the 30 days that followed the mainshock. The cumulative slip estimated from the repeaters and from the geodetic data differ in magnitude. The cumulative slip from the geodetic model is ∼60% of the slip estimated from the repeaters at the three areas. Such a difference could arise from the combination of several effects, like the empirical laws used to convert repeater magnitude into slip, the size of the cells to compute the slip from the repeater, the regularization constraints used in our inversion or an error in the elastic Green functions. The choice of the box size also has a large effect on the cumulative slip evolution.

5. Slip Rate Evolution

Most studies of afterslip so far have focused on the cumulative slip evolution and little attention has been paid on the dynamics over short periods. Our approach which solves for the slip rate offers the opportunity to test whether slip rate decreases smoothly in time or experiences pulses of slip at some areas of the fault. Figures 7a–7f show the spatial distribution of the afterslip rate at selected dates, from our smooth model. Figure 7g shows the afterslip moment rate together with the daily number of aftershocks for the smooth model. Because the cross-validation test suggests that rougher time evolution is resolved in the data, Figure 7h shows the afterslip moment rate from our rough model.

Velocity-strengthening response to stress increment predicts that high slip rate should decrease rapidly as $\frac{1}{t}$. The overall moment rate function shown in Figures 7g and 7h show such a rapid decay, with a moment rate decreasing by a factor of 3 after 10 days. Fitting a simple $\dot{s}_0/(1+t/\tau)$ function to the moment rate function of Figure 7g, we find a characteristic decay time of $\tau \sim 5$ days. Afterslip rate appears to be the largest at the northern patch (∼50 mm/day *versus* 25 mm/day for the deep and southern patches). The slip rate at the three patches decreases through time down to a few mm/day after 2.5 months. However, superimposed to the overall $\frac{1}{t}$ decay, an increase of the afterslip moment rate is observed around the period of occurrence of the largest aftershocks (Figures 7g and 7h), between 50 and 60 days after the mainshock. This period is also marked by an increase of the microseismicity daily rate (Figures 7g and 7h). In the following, we investigate in details the potential relationship between the afterslip and those large aftershocks.

5.1. Afterslip Behavior and the M_w 6.8, 7 November Deep Aftershock

The M_w 6.8 aftershock occurred on November 7, 51 days after the mainshock. The inversion of the static offset finds that it ruptured a 20×20 km^2 patch at 40 km depth, north of the deepest extent of the coseismic rupture (see Figure S6 in Supporting Information S1). Our cumulative afterslip model finds that this aftershock occurred in one of the three areas experiencing enhanced afterslip (Figure 5e). For that area, the afterslip rate model indicates that the slip rate decreases from ∼35 mm/day on the day after the mainshock down to less than 5 mm/day on October 29, that is 42 days after the mainshock (Figures 7a–7c). This value of slip rate is similar at the three areas of afterslip. However, from day 48 onward, while the slip rate continues to decrease at Boxes A and C (respectively north and south of the coseimic rupture), slip rate increases at the deepest part of Box B (the 31°S patch, Figure 7d). A maximum slip rate of ∼10 mm/day is found the day following the M_w 6.8 aftershock (Figure 7e), before decreasing during the next following 10 days.

The aftershock coseismic offset does not impact our inversion because time series of nearby GNSS sites have been split at the time of the aftershock to form independent observations and hence does not contribute to the modeled afterslip. However, the temporal smoothing constraints required to stabilize our inversion would tend to spread any daily sharp slip rate increment over a period of a few days. In order to evaluate this potential "time spreading" effect in our inversion and to better characterize the slip rate evolution around November 7, we

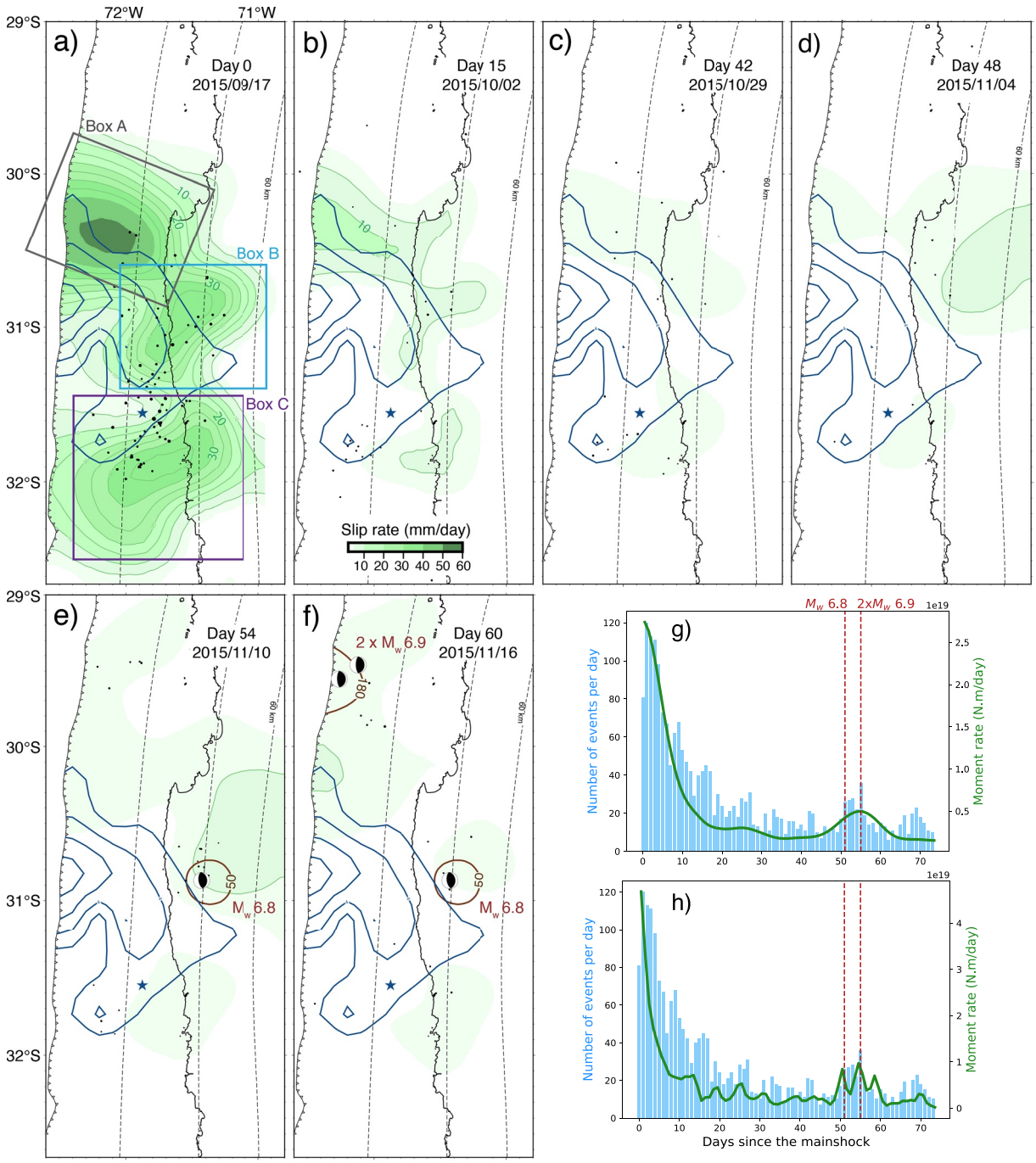

Figure 7. (a–f) Daily slip rate (smooth model) contoured in green every 5 mm/day (the first 3 mm/day of slip are hidden). The black dots are the seismicity occurring at the selected dates. Slip inversion results for the largest aftershocks on November 7 and November 11 are contoured in brown. The focal mechanisms are from GlobalCMT (Dziewonski et al., 1981; Ekström et al., 2012). The mainshock slip is contoured in blue every 2 m (Klein et al., 2017). The blue star is the M_w 8.3 2015 Illapel epicenter. The dashed lines are the Slab2.0 isodepths every 20 km (Hayes et al., 2018). Source time function of (g) the smooth model and (h) the rough model in green and events per day (CSN catalog) as blue bars. The vertical dashed lines in red are the aftershocks occurrence.

perform an inversion starting on September 17 but ending on November 7, the day before the aftershock. This inversion does not show any evidence of slip acceleration before the aftershock (Figure 8a). We then perform a second inversion starting on November 7 and ending on November 10. This latter inversion highlights localized rapid slip (~10 mm/day), encompassing the aftershock rupture area and rapidly decreasing to 4 mm/day the next day (Figures 8b and 8c).

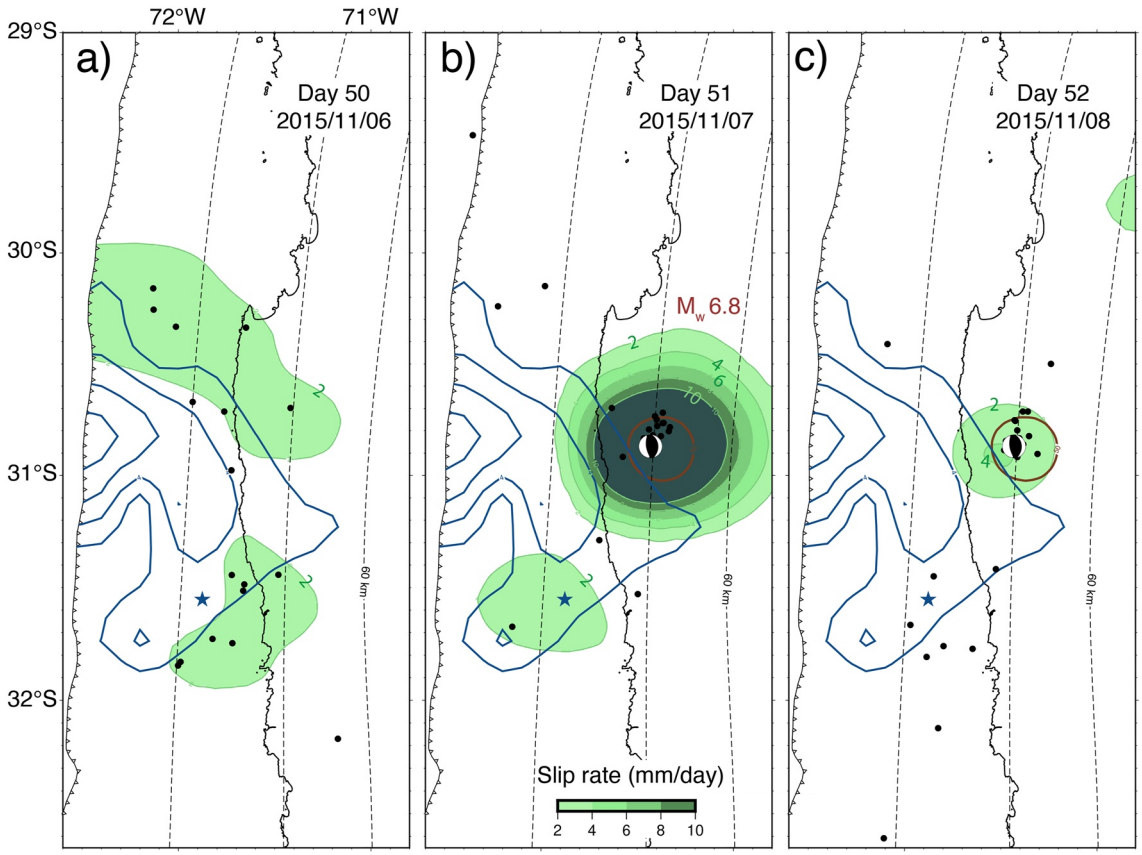

Figure 8. (a) Daily slip rate of an inversion ending on November 6. (b, c) Daily slip rate of inversion starting on November 7 and ending on November 10. The slip rate is contoured in green every 2 mm/day. The black dots are the seismicity occurring at the selected dates (CSN catalog). Slip inversion results for the M_w 6.8 on November 7 is contoured in brown. The mainshock slip is contoured in blue every 2 m (Klein et al., 2017). The blue star is the M_w 8.3 2015 Illapel epicenter. The focal mechanisms are from GlobalCMT (Dziewonski et al., 1981; Ekström et al., 2012). The dashed lines are the Slab2.0 isodepths every 20 km (Hayes et al., 2018).

We conclude that (a) the November 7 M_w 6.8 aftershock occurred in an area of enhanced afterslip compared to the neighbor area at the fault, (b) this aftershock generated its own local afterslip during a few days that superimposed to the overall evolution of the mainshock afterslip, (c) our inversion approach could capture the local slip rate increase from the small signal in the time series, that had not been seen in previous studies. However, the local slip acceleration is blurred in time because of the temporal constraints we imposed, whose optimal values were adjusted over the whole period of 2 months and all GNSS sites. Specifically "tuned" inversions can however overcome this limitation and can successfully image the local afterslip triggered by the aftershock.

5.2. Afterslip Behavior and the Two M_w 6.9, 11 November Shallow Aftershocks

The doublet of moderate size M_w 6.9 earthquakes occurred 55 days after the mainshock on November 11, at a distance of ∼100 km north of the mainshock rupture area (Figure S6 in Supporting Information S1). Both the remote location of these aftershocks with respect to the mainshock rupture area and the 55 days delay question whether they can be considered as aftershocks or not. Our kinematic inversion first reveals large afterslip developing north of the rupture and possibly at shallow depth. Our smooth geodetic afterslip model further finds that afterslip would have reached the area ruptured by the November 11 events (Figures 5e and 7e). This result is in agreement with Frank et al. (2017) who showed that the aftershocks front propagated fast and on a large distance at shallow depth, north of the rupture. Using the same procedure as for the deep November 7 aftershock, we tested whether the slight slip rate increase noted in Figure 7e actually occurred during the days preceding the two November 11 events. The inversion starting on November 7 (after the M_w 6.8 event) and ending on November 10 (before the M_w 6.9 events) does not show evidence for significant slip acceleration before November 11 (Figure 9a). We therefore believe that the small slip increase in Figure 7e rather reflects the local afterslip

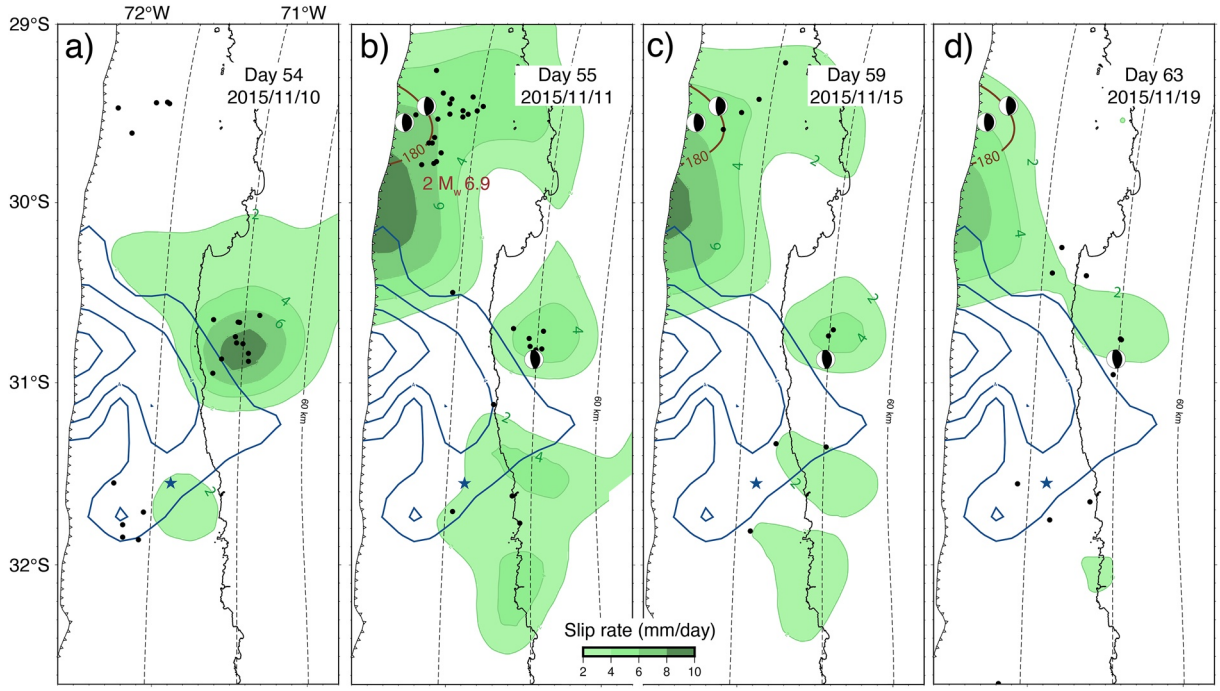

Figure 9. (a) Daily slip rate of an inversion starting on November 7 and ending on November 10. (b–d) Daily slip rate of an inversion starting on November 11. The slip rate is contoured in green every 2 mm/day. The black dots are the seismicity occurring at the selected dates (CSN catalog). Slip inversion results for the M_w 6.8 on November 7 and November 11 are contoured in brown. The focal mechanisms are from GlobalCMT (Dziewonski et al., 1981; Ekström et al., 2012). The mainshock slip is contoured in blue every 2 m (Klein et al., 2017). The blue star is the M_w 8.3 2015 Illapel epicenter. The dashed lines are the Slab2.0 isodepths every 20 km (Hayes et al., 2018).

induced by the November 7 earthquake. A small amount of afterslip is also noticed north of the November 11 earthquakes (Figure 7f) likely triggered by these earthquakes.

In order to confirm this view, we performed an inversion starting on November 11 (Figures 9b–9d), a few hours after the M_w 6.9 aftershocks. Despite some noise, this inversion clearly captures the shallow afterslip triggered by the two M_w 6.9 November 11 aftershocks. The aftershock-triggered afterslip area appears to be relatively large given the moderate magnitude of the two aftershocks (equivalent to a M_w 7.1). It is certainly not well resolved considering the large distance to the nearest GNSS sites, but the location of the found afterslip correlates pretty well with the location of the aftershocks triggered by the November 11 earthquakes (Figures 9b and 9c). The obtained model further clearly shows a slip rate decrease, for instance from 8 mm/day during the day of the aftershock down to 2 mm/day close to the aftershocks, a decrease rate consistent with the overall decay time estimated for the mainshock.

Interestingly, we also note that additional slip is suggested by our model for the deep patch. It also correlates with some seismicity activity possibly reflecting ongoing local afterslip following the November 7 aftershock (Figures 9a–9d).

In summary, we find that the largest aftershocks during the 74 days following the Illapel earthquake are linked with the afterslip evolution. The deepest one on November 7 probably corresponds to a locked asperity brought to failure by the surrounding afterslip. The 100 km remote distant and 2 months delayed aftershocks were likely triggered by the large amount of afterslip north of the coseismic rupture.

5.3. A Slow Slip Event at the Southern Patch?

The rougher afterslip model shows additional modulations of the moment rate, which are not related to the occurrence of any significant aftershock, but correlates with an increase of the seismicity rate (Figure 7h). By inspection of Movie S4 in Supporting Information S1, we do not find a clear spatial correlation between the seismicity rate and the local slip rate increase neither around day 19 nor day 25. However, from day 67 onward, the slip rate increases at the southern patch of afterslip at ~25 km depth. The slip rate culminates with more than 5 mm/day

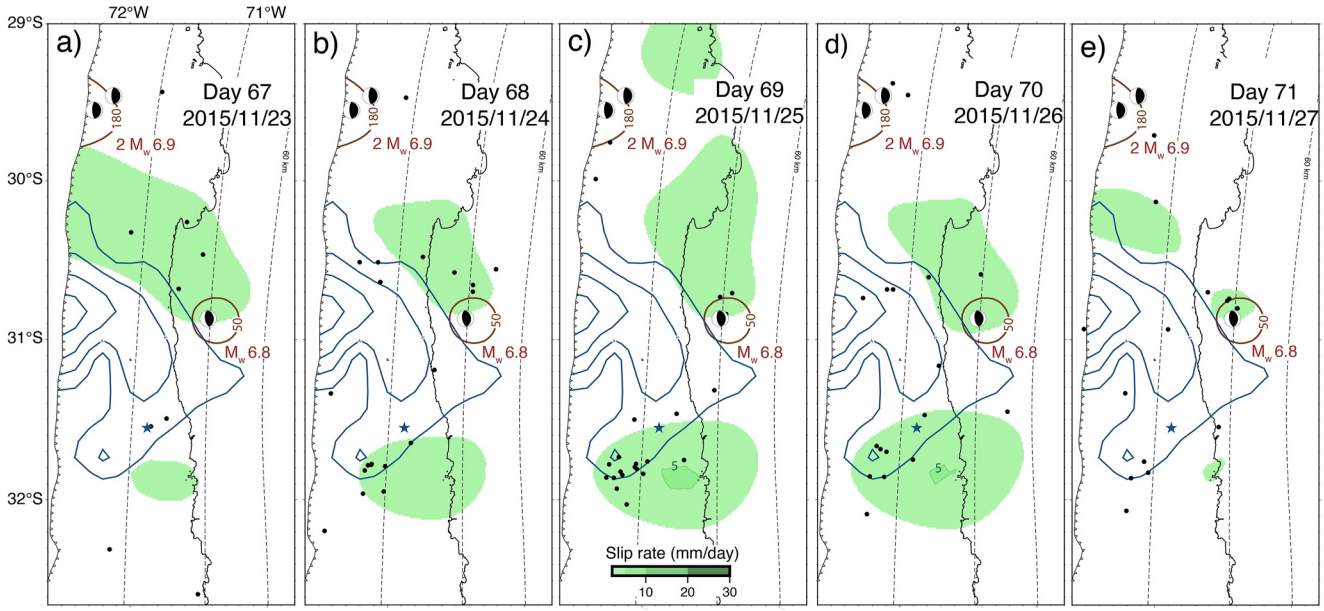

Figure 10. (a–e) Daily slip rate (rough model) of the afterslip modulation south of the mainshock at selected dates. The slip rate is contoured in green every 5 mm/day (the first 3 mm/day of slip are hidden). The black dots are the seismicity occurring at the selected dates (CSN catalog). Slip inversion results for the largest aftershocks on November 7 and November 11 are contoured in brown. The focal mechanisms are from GlobalCMT (Dziewonski et al., 1981; Ekström et al., 2012). The mainshock slip is contoured in blue every 2 m (Klein et al., 2017). The blue star is the M_w 8.3 2015 Illapel epicenter. The dashed lines are the Slab2.0 isodepths every 20 km (Hayes et al., 2018).

of slip observed on day 69. After this day, the slip rate slowly decreases until it vanishes on day 72 (Figure 10). We find that this potential 6-day slow slip correlates with a local seismicity increase at the tip of the transient slip area. The synthetic test shown in Movie S6 in Supporting Information S1 suggests that the data can resolve very small transient signal over a few days. Here, the equivalent moment released through the suspected transient is M_w 6.1–6.2. This is indeed very small, but the correlation with the increase of seismicity simultaneously in space and time is a strong support for the hypothesis of a slow slip event superimposed to the overall afterslip evolution. The comparison with the interseismic regime described in Section 7.3 indicates that this area of the subduction interface is prone to regular slow slip events and seismic swarms.

6. Discussion

6.1. Overall Pattern of Afterslip

Overall, our results confirm previous findings of immediate relocking of the coseismically ruptured area and afterslip developing at the edge of the coseismic rupture. Our kinematic inversion finds the logarithm evolution of the cumulative slip and the $\frac{1}{t}$ decrease of the slip rate with a characteristic decay time of ~5 days. The cumulative moment of afterslip is 2.37×10^{20} N.m after a month, equivalent to a M_w 7.5, a value similar to Barnhart et al. (2016) and Huang et al. (2017). After 74 days, the cumulative moment of afterslip is 3.53×10^{20} N.m equivalent to a M_w 7.6, corresponding to 13% of the coseismic moment. Compared to previous studies, our model finds that, rather than taking place homogeneously around the rupture, afterslip develops from relatively localized areas. No afterslip developed downdip the deep edge of the coseismic rupture and the afterslip located north of the rupture is the largest. Aside this overall behavior, there are specific patterns that we discuss in the next paragraphs.

6.2. Afterslip Within the Coseismic Rupture Area

An average of ~3–4 m of coseismic slip is imaged by all coseismic models (Barnhart et al., 2016; Klein et al., 2017; Melgar et al., 2016; Ruiz et al., 2016; Shrivastava et al., 2016) at a 30–45 km deep patch. Our model infers significant afterslip at latitude 31.2°S (~30 km depth) reaching 40 cm, well inside the coseismic rupture (western half of Box B in Figure 5g and southwest of Box 2 in Figure 6a). Given its dimension (~40×20 km^2), the vicinity of the coastline and the direct observation from dense GNSS data for both coseismic and afters-

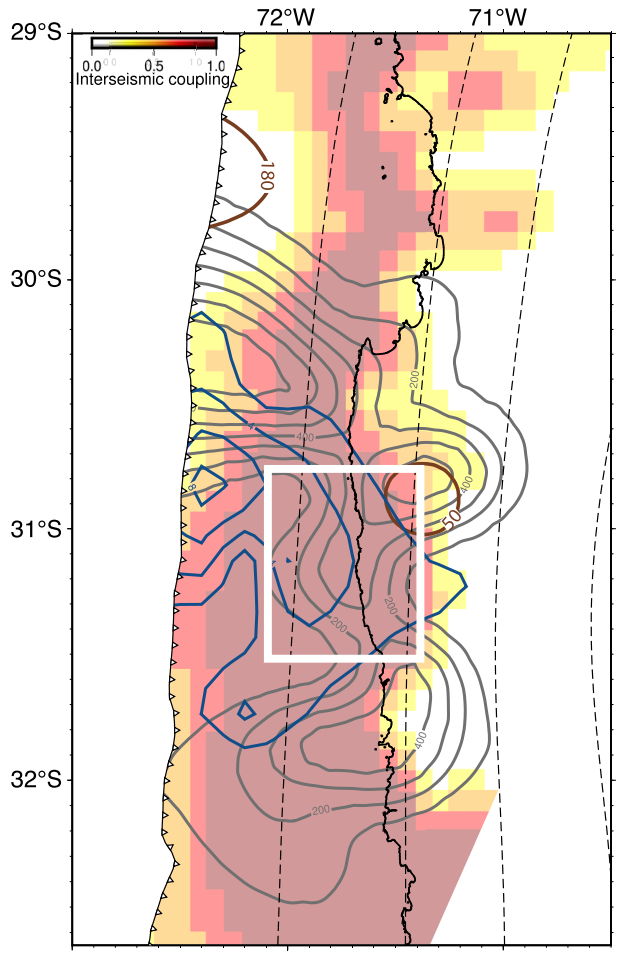

Figure 11. Comparison of the 74 days cumulative afterslip smooth model contoured in gray from 20 cm and then every 10 cm with the interseismic coupling of Métois et al. (2014). The white rectangle is the overlapping area with the coseismic rupture. The mainshock slip is contoured in blue every 2 m (Klein et al., 2017). Slip inversion results for the largest aftershocks on November 7 and November 11 are contoured in brown. The dashed lines are the Slab2.0 depths every 20 km (Hayes et al., 2018).

lip models, this overlap is certainly resolved. In addition, that area hosts a significant density of aftershocks (Figure 6c, Frank et al., 2017) and among them a significant number of repeating earthquakes (Figure 6b, Huang et al., 2017), providing additional evidences for aseismic slip at this location. Overlap of afterslip with coseismic slip is also found at shallow depth at the northern edge of the coseismic rupture (southwestern part of Box A in Figure 5g and west of Box 1 in Figure 6a). This is an area where a relatively large distance from the coast prevents the precise location and amount of slip to be retrieved from the inversion, making this overlap speculative. We therefore conclude that although most of the afterslip occurred at the edge of the coseismic rupture area and most of the seismically rupture appears to have fully relocked quickly, a ~40 × 20 km^2 region (western half of Box B in Figure 5g and southwest of Box 2 in Figure 6a) slip seismically and continued to slip aseismically during the weeks following the mainshock. The area of afterslip within the coseismic rupture is adjacent to the area found to have slipped seismically through large aftershocks during the first 6 hr following the mainshock by Twardzik et al. (2021). It might therefore also include the afterslip generated by these aftershocks. However, the time evolution of afterslip at that area (Box 2 in Figure 6e) does not show slower or faster decay with respect to the other areas of afterslip (Boxes 1 and 3, Figures 6d and 6f).

The observation of significant afterslip taking place within the coseismic area of the mainshock is somehow at odds with the asperity model described in the introduction of the paper, where seismic rupture occurs at velocity-weakening areas of the fault, while afterslip witnesses velocity-strengthening friction. Both earthquake rupture dynamic simulations (Kaneko et al., 2010; Noda & Lapusta, 2013) and observations (Harris, 2017) show that seismic ruptures can propagate into velocity-strengthening areas of faults, through dynamic weakening induced by high shear stress as the seismic rupture front arrives at the edge of a velocity-strengthening area. This mechanism possibly happened during the Illapel earthquake. Aochi and Ruiz (2021) proposed that the Illapel earthquake started with a foreshock and that the rupture immediately propagated northward, similarly as observed in the back-projection and the kinematic slip inversions (*e.g.*, Melgar et al., 2016). The epicentral area experienced 3–4 m of slip during the first 30 s of the rupture, before reaching the future afterslip area which broke between 30 and 40 s, before propagating further northward and updip. We speculate that this area is velocity-strengthening that would explain the observed afterslip and that it resisted the seismic rupture propagation during the Illapel earthquake, as in the models proposed by Kaneko et al. (2010).

6.3. Comparison With the Interseismic Coupling Map and 1992–2015 Microseismicity

Interseismic coupling map derived from years before the Illapel earthquake shows rather spatial homogeneous coupling (>60%) between 10 and 45 km depth (Métois et al., 2014), much smoother than the afterslip distribution imaged from our inversions (Figure 11). The deepest areas of afterslip correlate with the downdip limit of high interseismic coupling. The northern patch of afterslip also correlates with weaker interseismic coupling for our smoother model. However, the afterslip area that occurred within the seismically ruptured area (white rectangle in Figure 11) shows high coupling, perhaps because it lies in the stress shadow of both updip and downdip locked area. The southern patch of afterslip is located in a large area of high coupling. This area is located close to the coastline so it is expected to be well resolved for both our afterslip models and the interseismic coupling model. This observation is at odds with the asperity model. A similar observation has been made for the Ecuador M_w 7.8 2016 earthquake for one patch of afterslip (Rolandone et al., 2018). In Rolandone et al. (2018), the patch that was locked during the years before the earthquake was found to host regular Slow Slip Events (SSE) and Seismic Swarms (SS).

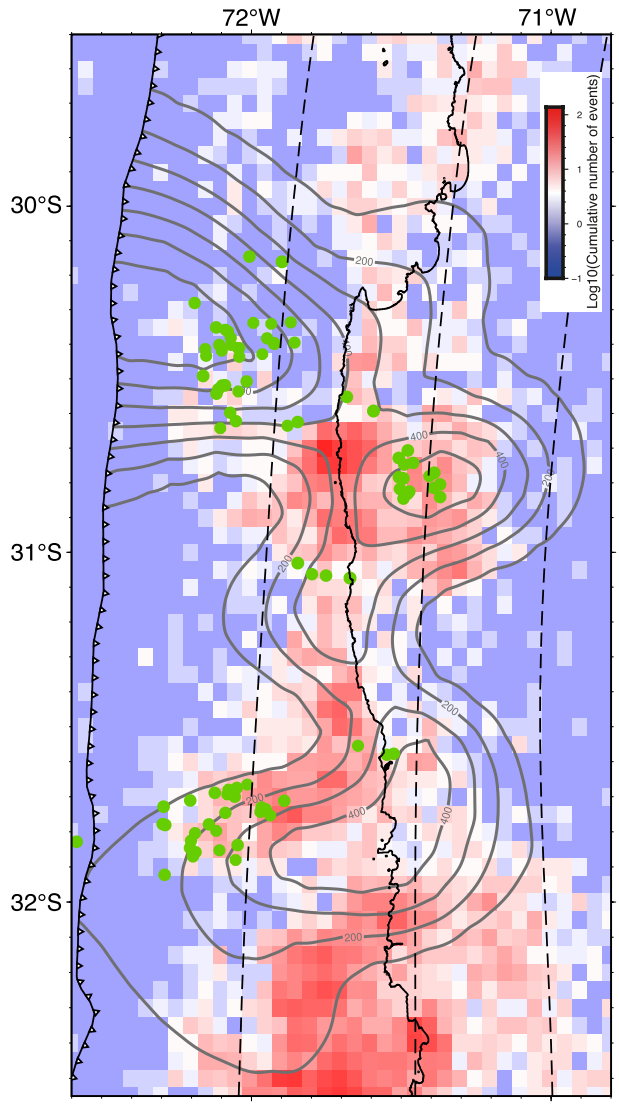

Figure 12. Comparison of the 74 days cumulative afterslip smooth model with the interseismic seismicity (Poli et al., 2017). The green dots are the repeater earthquakes locations of Poli et al. (2017). The dashed lines are the Slab2.0 depths every 20 km (Hayes et al., 2018).

Along the Illapel segment of the Chilean subduction zone, no SSE has been geodetically evidenced yet, possibly due to a lack of a dense permanent monitoring network. However, Poli et al. (2017) studied the seismicity during the 20 years preceding the Illapel earthquake and identified regular seismic swarms. Seismic swarms occur at three distinct areas at the megathrust showing a striking correlation with both our afterslip models and the aftershocks locations (Figure 12). The first area of seismic swarm at latitudes 30.6°–31°S matches the patch of enhanced afterslip where the November 7 aftershock occurred. The second area at latitudes 31.3°–31.9°S is at the edges of the afterslip in our models. Finally, the last one located at latitudes 31.9°–32.6°S is at the periphery of our afterslip model. Poli et al. (2017) further show that repeating earthquakes occur during seismic swarms, witnessing associated SSEs. The location of the repeaters found Poli et al. (2017) is found to occur at the periphery of the afterslip areas of our rough geodetic afterslip model. Such correlation between the location of enhanced afterslip and areas experiencing SSEs and SS is very similar to the one observed for the Pedernales 2016 earthquake in Ecuador (Rolandone et al., 2018). It confirms a key-role of SSEs and SS areas in stopping the seismic rupture for large earthquakes (Vaca et al., 2018) and in promoting afterslip. Afterslip and SSEs occurring at the same location has also been observed in the Nicoya peninsula, Costa Rica (Hobbs et al., 2017).

Poli et al. (2017) noticed that the spatial clustering of the seismic activity before the Illapel earthquake shares similar orientation with the main fracture zones observed on the outer rise of the subducting Nazca plate. Therefore, they propose that areas of the megathrust experiencing seismic swarms correspond to fractures within the subducted Nazca slab, characterized by high pore-fluid pressure and frequent fluid releases. High pore pressure reduces the normal stress, favors stress release through transient aseismic slip during the interseismic phase and through afterslip after a nearby large rupture.

6.4. A Highly Dynamic Afterslip

While the cumulative afterslip evolution shows a smooth increase, the afterslip rate evolution shows higher dynamics in space and time. Our modeling suggests that the data not only carry information about the overall location of afterslip, but also includes information about the high frequency dynamics of afterslip. This high frequency dynamics is also suggested by the days-long modulation in the microseismicity rate (Movies S4 and S6 in Supporting Information S1).

Large aftershocks appear to occur at area or at the edge of enhanced afterslip. These large aftershocks in turn trigger their own, local afterslip that superimposes to the overall mainshock-induced afterslip. Our approach made possible to identify such modulations, but with the limitation of the smoothing in time of the actual slip rate. Nonetheless, specific inversions at selected time windows were able to capture the local afterslip of the November 7 M_w 6.8 and the two November 11 M_w 6.9 earthquakes and their time evolution.

Aside from aftershocks, our rough model highlights a small afterslip rate modulation south of the coseismic rupture. We suggest that this afterslip modulation is a small slow slip event (SSE). Indeed, the observed slip shows a progressive slip acceleration and decrease as SSEs do. The proposed magnitude of M_w 6.1–6.2 for a duration of 5–6 days agrees with scaling laws proposed for SSE (Ide et al., 2007). Finally, it occurred at a location of the interface where regular seismic swarms, most probably associated with SSEs have been documented prior the 2015 Illapel earthquake (Poli et al., 2017).

These modulations remain small compared to the afterslip, and do not challenge the general view that the mainshock coseismic stress increment drives the overall pattern of afterslip. They however suggest that some other

processes are superimposed to it. 10 km scale locked asperities locally resist to the aseismic slip around or at the edge of them, until the shear stress from both the mainshock coseismic slip and afterslip leads them to break. Then these aftershocks locally trigger their own afterslip, possibly helping the overall afterslip to propagate farther. Interpreting SSE is more challenging since they are often associated with velocity-weakening behavior (*e.g.*, Rubin, 2008). Perhaps, following Poli et al. (2017)' suggestion made for the interseismic period, relatively sudden pore pressure change due to fluid injection might provide an explanation to be explored in future.

7. Conclusions

A full time-dependent inversion of both cGNSS and sGNSS provides a kinematic view of the 74-day afterslip that developed during 2 months after the Illapel M_w 8.3 megathrust earthquake. It highlights that afterslip developed at preferential areas at the subduction interface, which had experienced regular seismic swarms and likely slow slip events during the decades preceding the earthquake. Those areas possibly correspond to fractures within the slab that promote high pore pressure and are favorable to aseismic slip. Such areas prevented the rupture to extend along strike at their locations. Afterslip and SSEs are usually thought to witness different friction laws at the megathrust. Here, they appear to take place at the same location, certainly obeying the same friction law. This observation is not accounted for in the "rate-state asperity" model, but it might be key in anticipating the extent of future larges ruptures.

Our detailed modeling further suggests a close link between afterslip and large aftershocks. Ten kilometers of scale locked asperities might be brought to failure by the afterslip developing in their vicinity, in addition to the stress increment induced by the mainshock. This process might explain remote and delayed moderate size aftershocks as our results suggest for the two M_w 6.9 events on November 11, 2015. Relationship between a large aftershock and afterslip propagation was recently observed for a M_w 6.9 earthquake in central Chile (Klein et al., 2021). Hence, survey of afterslip evolution after a large earthquakes might therefore help to define preferential location for large aftershocks to occur.

For the first time, our study images the afterslip rate evolution and highlights that the afterslip is highly dynamic, like the seismicity. GNSS sites are able to capture the afterslip of the large aftershocks and a slow slip event, south of the mainshock rupture. This slow slip event correlates with an increase of microseismicity rate.

Those observations are similar to the one made after the M_w 7.8 2016 Ecuador earthquake (Nocquet et al., 2017). Two large M_w 6.7–6.9 aftershocks occurred a month after the mainshock in an area of enhanced afterslip having experienced regular seismic swarms and slow slip events *prior* the earthquake (Rolandone et al., 2018; Vaca et al., 2018). A similar pattern was also observed after the M_w 7.6 2012 Nicoya earthquake at least updip the rupture (Dixon et al., 2014; Hobbs et al., 2017; Voss et al., 2017). These similarities suggest a common behavior, perhaps corresponding to the seismic behavior of the highly heterogeneous subduction interface.

Data Availability Statement

The GNSS data used in this study are the Data Set S1. The continuous GNSS data solution is regularly updated, for more information please refer to Klein et al. (2022). The kinematic slip inversion code (Nocquet, 2022) is available on Zenodo at https://zenodo.org/record/7467256#.Y6Ljb7KZNb8.

Acknowledgments
RT PhD was funded by the Ministère de l'Enseignement supérieur, de la Recherche et de l'Innovation. This research was supported by the French Agence National de la Recherche (ANR) through the project S5 (Grant ANR-19-CE31-0003-01). JO acknowledges support from the ANID scholarship ANID-PFCHA/Doctorado Nacional/2020-21200903. SR thanks ANID/FONDECYT; project 1200779. Numerical computations were partly performed on the S-CAPAD platform, IPGP, France. Figures were made using Global Mapping Tools (GMT) version 6 (Wessel et al., 2019). We thank two anonymous reviewers for their suggestions that helped to improve the manuscript.

References

Agurto, H., Rietbrock, A., Ryder, I., & Miller, M. (2012). Seismic-afterslip characterization of the 2010 Mw 8.8 Maule, Chile, earthquake based on moment tensor inversion. *Geophysical Research Letters*, *39*, L20303. https://doi.org/10.1029/2012GL053434

Aochi, H., & Ruiz, S. (2021). Early stage and main ruptures of the 2015 Mw8.3 Illapel, Chile, megathrust earthquake: Kinematic elliptical inversions and dynamic rupture simulations. *Journal of Geophysical Research: Solid Earth*, *126*, e2020JB021207. https://doi.org/10.1029/2020JB021207

Avouac, J.-P. (2015). From geodetic imaging of seismic and aseismic fault slip to dynamic modeling of the seismic cycle. *Annual Review of Earth and Planetary Sciences*, *43*(1), 233–271. https://doi.org/10.1146/annurev-earth-060614-105302

Baez, J. C., Leyton, F., Troncoso, C., del Campo, F., Bevis, M., Vigny, C., et al. (2018). The Chilean GNSS network: Current status and progress toward early warning applications. *Seismological Research Letters*, *89*(4), 1546–1554. https://doi.org/10.1785/0220180011

Barnhart, W. D., Murray, J. R., Briggs, R. W., Gomez, F., Miles, C. P., Svarc, J., et al. (2016). Coseismic slip and early afterslip of the 2015 Illapel, Chile, earthquake: Implications for frictional heterogeneity and coastal uplift. *Journal of Geophysical Research: Solid Earth*, *121*, 6172–6191. https://doi.org/10.1002/2016JB013124

Bedford, J., Moreno, M., Baez, J. C., Lange, D., Tilmann, F., Rosenau, M., et al. (2013). A high-resolution, time-variable afterslip model for the 2010 Maule Mw=8.8, Chile megathrust earthquake. *Earth and Planetary Science Letters*, *383*, 26–36. https://doi.org/10.1016/j.epsl.2013.09.020

Blewitt, G., Kreemer, C., Hammond, W. C., & Gazeaux, J. (2016). Midas robust trend estimator for accurate GPS station velocities without step detection. *Journal of Geophysical Research: Solid Earth*, *121*, 2054–2068. https://doi.org/10.1002/2015JB012552

Chalumeau, C., Agurto-Detzel, H., De Barros, L., Charvis, P., Galve, A., Rietbrock, A., et al. (2021). Repeating earthquakes at the edge of the after-slip of the 2016 Ecuadorian Mw 7.8 Pedernales earthquake. *Journal of Geophysical Research: Solid Earth*, *126*, e2021JB021746. https://doi.org/10.1029/2021JB021746

Dixon, T. H., Jiang, Y., Malservisi, R., McCaffrey, R., Voss, N., Protti, M., & Gonzalez, V. (2014). Earthquake and tsunami forecasts: Relation of slow slip events to subsequent earthquake rupture. *Proceedings of the National Academy of Sciences of the United States of America*, *111*(48), 17039–17044. https://doi.org/10.1073/pnas.1412299111

Dziewonski, A. M., Chou, T.-A., & Woodhouse, J. H. (1981). Determination of earthquake source parameters from waveform data for studies of global and regional seismicity. *Journal of Geophysical Research*, *86*(B4), 2825–2852. https://doi.org/10.1029/JB086iB04p02825

Ekström, G., Nettles, M., & Dziewoński, A. (2012). The global CMT project 2004–2010: Centroid-moment tensors for 13,017 earthquakes. *Physics of the Earth and Planetary Interiors*, *200*, 1–9. https://doi.org/10.1016/j.pepi.2012.04.002

Feng, W., Samsonov, S., Tian, Y., Qiu, Q., Li, P., Zhang, Y., et al. (2017). Surface deformation associated with the 2015 Mw 8.3 Illapel earthquake revealed by satellite-based geodetic observations and its implications for the seismic cycle. *Earth and Planetary Science Letters*, *460*, 222–233. https://doi.org/10.1016/j.epsl.2016.11.018

Frank, W. B., Poli, P., & Perfettini, H. (2017). Mapping the rheology of the Central Chile subduction zone with aftershocks. *Geophysical Research Letters*, *44*, 5374–5382. https://doi.org/10.1002/2016GL072288

Freymueller, J., King, N., & Segall, P. (1994). The co-seismic slip distribution of the Landers earthquake. *Bulletin of the Seismological Society of America*, *84*(3), 646–659. https://doi.org/10.1785/bssa0840030646

Hansen, P. C. (1992). Analysis of discrete ill-posed problems by means of the L-curve. *SIAM Review*, *34*(4), 561–580. https://doi.org/10.1137/1034115

Harris, R. A. (2017). Large earthquakes and creeping faults. *Reviews of Geophysics*, *55*, 169–198. https://doi.org/10.1002/2016RG000539

Hayes, G. P., Moore, G. L., Portner, D. E., Hearne, M., Flamme, H., Furtney, M., & Smoczyk, G. M. (2018). Slab2, a comprehensive subduction zone geometry model. *Science*, *362*(6410), 58–61. https://doi.org/10.1126/science.aat4723

Hobbs, T., Kyriakopoulos, C., Newman, A., Protti, M., & Yao, D. (2017). Large and primarily updip afterslip following the 2012 Mw 7.6 Nicoya, Costa Rica earthquake. *Journal of Geophysical Research: Solid Earth*, *122*, 5712–5728. https://doi.org/10.1002/2017JB014035

Hsu, Y.-J., Simons, M., Avouac, J.-P., Galetzka, J., Sieh, K., Chlieh, M., et al. (2006). Frictional afterslip following the 2005 Nias-Simeulue earthquake, Sumatra. *Science*, *312*(5782), 1921–1926. https://doi.org/10.1126/science.1126960

Huang, H., Xu, W., Meng, L., Bürgmann, R., & Baez, J. C. (2017). Early aftershocks and afterslip surrounding the 2015 Mw 8.4 Illapel rupture. *Earth and Planetary Science Letters*, *457*, 282–291. https://doi.org/10.1016/j.epsl.2016.09.055

Ide, S., Beroza, G. C., Shelly, D. R., & Uchide, T. (2007). A scaling law for slow earthquakes. *Nature*, *447*(7140), 76–79. https://doi.org/10.1038/nature05780

Johnson, K. M., Fukuda, J., & Segall, P. (2012). Challenging the rate-state asperity model: Afterslip following the 2011 M9 Tohoku-Oki, Japan, earthquake. *Geophysical Research Letters*, *39*, L20302. https://doi.org/10.1029/2012GL052901

Kaneko, Y., Avouac, J.-P., & Lapusta, N. (2010). Towards inferring earthquake patterns from geodetic observations of interseismic coupling. *Nature Geoscience*, *3*(5), 363–369. https://doi.org/10.1038/ngeo843

Klein, E., Potin, B., Pasten-Araya, F., Tissandier, R., Azua, K., Duputel, Z., et al. (2021). Interplay of seismic and a-seismic deformation during the 2020 sequence of Atacama, Chile. *Earth and Planetary Science Letters*, *570*, 117081. https://doi.org/10.1016/j.epsl.2021.117081

Klein, E., Vigny, C., Fleitout, L., Grandin, R., Jolivet, R., Rivera, E., & Métois, M. (2017). A comprehensive analysis of the Illapel 2015 Mw8.3 earthquake from GPS and InSAR data. *Earth and Planetary Science Letters*, *469*, 123–134. https://doi.org/10.1016/j.epsl.2017.04.010

Klein, E., Vigny, C., Nocquet, J.-M., & Boulze, H. (2022). A 20 year-long GNSS solution across South America with focus in Chile. *Bulletin de la Société Géologique de France*, *193*(1), 5. https://doi.org/10.1051/bsgf/2022005

Kositsky, A., & Avouac, J.-P. (2010). Inverting geodetic time series with a principal component analysis-based inversion method. *Journal of Geophysical Research*, *115*, B03401. https://doi.org/10.1029/2009JB006535

Lay, T., & Kanamori, H. (1981). An asperity model of large earthquake sequences. *Earthquake Prediction: An International Review*, *4*, 579–592.

Liu, K., Geng, J., Wen, Y., Ortega-Culaciati, F., & Comte, D. (2022). Very early postseismic deformation following the 2015 Mw 8.3 Illapel earthquake, Chile revealed from kinematic GPS. *Geophysical Research Letters*, *49*, e2022GL098526. https://doi.org/10.1029/2022GL098526

Matthews, M. V., & Segall, P. (1993). Estimation of depth-dependent fault slip from measured surface deformation with application to the 1906 san francisco earthquake. *Journal of Geophysical Research*, *98*(B7), 12153–12163. https://doi.org/10.1029/93JB00440

Melgar, D., Fan, W., Riquelme, S., Geng, J., Liang, C., Fuentes, M., et al. (2016). Slip segmentation and slow rupture to the trench during the 2015, Mw8.3 Illapel, Chile earthquake. *Geophysical Research Letters*, *43*, 961–966. https://doi.org/10.1002/2015GL067369

Métois, M., Vigny, C., Socquet, A., Delorme, A., Morvan, S., Ortega, I., & Valderas-Bermejo, C.-M. (2014). GPS-derived interseismic coupling on the subduction and seismic hazards in the Atacama region, Chile. *Geophysical Journal International*, *196*(2), 644–655. https://doi.org/10.1093/gji/ggt418

Nadeau, R. M., & Johnson, L. R. (1998). Seismological studies at Parkfield VI: Moment release rates and estimates of source parameters for small repeating earthquakes. *Bulletin of the Seismological Society of America*, *88*(3), 790–814. https://doi.org/10.1785/bssa0880030790

Nikkhoo, M., & Walter, T. R. (2015). Triangular dislocation: An analytical, artefact-free solution. *Geophysical Journal International*, *201*(2), 1119–1141. https://doi.org/10.1093/gji/ggv035

Nocquet, J.-M. (2018). Stochastic static fault slip inversion from geodetic data with non-negativity and bound constraints. *Geophysical Journal International*, *214*(1), 366–385. https://doi.org/10.1093/gji/ggy146

Nocquet, J.-M. (2022). Pyeq: A software for fault slip kinematic inversion from GNSS time series. *Zenodo*. (Funding agency: Agence Nationale de la Recherche (ANR), Grant number: ANR-19-CE31-0003-01). https://doi.org/10.5281/zenodo.7467256

Nocquet, J.-M., Jarrin, P., Vallée, M., Mothes, P. A., Grandin, R., Rolandone, F., et al. (2017). Supercycle at the Ecuadorian subduction zone revealed after the 2016 Pedernales earthquake. *Nature Geoscience*, *10*(2), 145–149. https://doi.org/10.1038/ngeo2864

Noda, H., & Lapusta, N. (2013). Stable creeping fault segments can become destructive as a result of dynamic weakening. *Nature*, *493*(7433), 518–521. https://doi.org/10.1038/nature11703

Page, M. T., Custódio, S., Archuleta, R. J., & Carlson, J. (2009). Constraining earthquake source inversions with GPS data: 1. Resolution-based removal of artifacts. *Journal of Geophysical Research*, *114*, B01314. https://doi.org/10.1029/2007JB005449

Perfettini, H., & Avouac, J.-P. (2004). Postseismic relaxation driven by brittle creep: A possible mechanism to reconcile geodetic measurements and the decay rate of aftershocks, application to the chi-chi earthquake, Taiwan. *Journal of Geophysical Research*, *109*, B02304. https://doi.org/10.1029/2003JB002488

Perfettini, H., Avouac, J.-P., Tavera, H., Kositsky, A., Nocquet, J.-M., Bondoux, F., et al. (2010). Seismic and aseismic slip on the Central Peru megathrust. *Nature*, *465*(7294), 78–81. https://doi.org/10.1038/nature09062

Piñón, D. A., Gómez, D. D., Smalley, R., Jr., Cimbaro, S. R., Lauría, E. A., & Bevis, M. G. (2018). The history, state, and future of the Argentine continuous satellite monitoring network and its contributions to geodesy in Latin America. *Seismological Research Letters*, *89*(2A), 475–482. https://doi.org/10.1785/0220170162

Poli, P., Maksymowicz, A., & Ruiz, S. (2017). The Mw 8.3 Illapel earthquake (Chile): Preseismic and postseismic activity associated with hydrated slab structures. *Geology*, *45*(3), 247–250. https://doi.org/10.1130/g38522.1

Rolandone, F., Nocquet, J.-M., Mothes, P. A., Jarrin, P., Vallée, M., Cubas, N., et al. (2018). Areas prone to slow slip events impede earthquake rupture propagation and promote afterslip. *Science Advances*, *4*(1), eaao6596. https://doi.org/10.1126/sciadv.aao6596

Rubin, A. M. (2008). Episodic slow slip events and rate-and-state friction. *Journal of Geophysical Research*, *113*, B11414. https://doi.org/10.1029/2008JB005642

Ruiz, S., Klein, E., del Campo, F., Rivera, E., Poli, P., Metois, M., et al. (2016). The seismic sequence of the 16 September 2015 Mw 8.3 Illapel, Chile, earthquake. *Seismological Research Letters*, *87*(4), 789–799. https://doi.org/10.1785/0220150281

Ruiz, S., & Madariaga, R. (2018). Historical and recent large megathrust earthquakes in Chile. *Tectonophysics*, *733*, 37–56. https://doi.org/10.1016/j.tecto.2018.01.015

Shrivastava, M. N., González, G., Moreno, M., Chlieh, M., Salazar, P., Reddy, C., et al. (2016). Coseismic slip and afterslip of the 2015 Mw 8.3 Illapel (Chile) earthquake determined from continuous GPS data. *Geophysical Research Letters*, *43*, 10710–10719. https://doi.org/10.1002/2016GL070684

Tian, Z., Freymueller, J. T., & Yang, Z. (2020). Spatio-temporal variations of afterslip and viscoelastic relaxation following the mw 7.8 Gorkha (Nepal) earthquake. *Earth and Planetary Science Letters*, *532*, 116031. https://doi.org/10.1016/j.epsl.2019.116031

Tsang, L. L., Vergnolle, M., Twardzik, C., Sladen, A., Nocquet, J.-M., Rolandone, F., et al. (2019). Imaging rapid early afterslip of the 2016 Pedernales earthquake, Ecuador. *Earth and Planetary Science Letters*, *524*, 115724. https://doi.org/10.1016/j.epsl.2019.115724

Twardzik, C., Vergnolle, M., Sladen, A., & Tsang, L. L. (2021). Very early identification of a bimodal frictional behavior during the post-seismic phase of the 2015 Mw 8.3 Illapel, Chile, earthquake. *Solid Earth Discussions*, 12, 2523–2537. https://doi.org/10.5194/se-12-2523-2021

Vaca, S., Vallée, M., Nocquet, J.-M., Battaglia, J., & Régnier, M. (2018). Recurrent slow slip events as a barrier to the northward rupture propagation of the 2016 Pedernales earthquake (Central Ecuador). *Tectonophysics*, *724*, 80–92. https://doi.org/10.1016/j.tecto.2017.12.012

Vigny, C., Rudloff, A., Ruegg, J. C., Madariaga, R., Campos, J., & Alvarez, M. (2009). Upper plate deformation measured by GPS in the Coquimbo Gap, Chile. *Physics of the Earth and Planetary Interiors*, *175*(1), 86–95. https://doi.org/10.1016/j.pepi.2008.02.013

Voss, N. K., Malservisi, R., Dixon, T. H., & Protti, M. (2017). Slow slip events in the early part of the earthquake cycle. *Journal of Geophysical Research: Solid Earth*, *122*, 6773–6786. https://doi.org/10.1002/2016JB013741

Wessel, P., Luis, J., Uieda, L., Scharroo, R., Wobbe, F., Smith, W. H., & Tian, D. (2019). The generic mapping tools version 6. *Geochemistry, Geophysics, Geosystems*, *20*, 5556–5564. https://doi.org/10.1029/2019GC008515

Xiang, Y., Yue, J., Jiang, Z., & Xing, Y. (2021). Spatial–temporal properties of afterslip associated with the 2015 Mw 8.3 Illapel earthquake, Chile. *Earth Planets and Space*, *73*(1), 1–15. https://doi.org/10.1186/s40623-021-01367-7